Paleoceanography and Paleoclimatology

RESEARCH ARTICLE
10.1029/2022PA004438

The Impact of Different Atmospheric CO_2 Concentrations on Large Scale Miocene Temperature Signatures

Akil Hossain[1], Gregor Knorr[1], Wilfried Jokat[1,2], Gerrit Lohmann[1,3], Katharina Hochmuth[4,5], Paul Gierz[1], Karsten Gohl[1], and Christian Stepanek[1]

[1]Alfred Wegener Institute, Helmholtz-Centre for Polar and Marine Research, Bremerhaven, Germany, [2]Department of Geoscience, University of Bremen, Bremen, Germany, [3]MARUM & Department of Environmental Physics, University of Bremen, Bremen, Germany, [4]School of Geography, Geology and the Environment, University of Leicester, Leicester, UK, [5]Australian Center of Excellence in Antarctic Science, Institute of Marine and Antarctic Studies, University of Tasmania, Hobart, Tas, Australia

Key Points:

- At a CO_2 level of 450 ppm, a Miocene simulation shows a global mean surface warming of +3.1°C relative to the preindustrial state
- Atmospheric CO_2 increase from 280 to 450 ppm causes a warming of ∼1.4°C, which is as strong as all other forcing factors combined
- At higher atmospheric CO_2 levels, the Miocene climate shows a reduced polar amplification linked to a breakdown of seasonality in the Arctic

Supporting Information:

Supporting Information may be found in the online version of this article.

Correspondence to:

A. Hossain,
akil.hossain@awi.de

Citation:

Hossain, A., Knorr, G., Jokat, W., Lohmann, G., Hochmuth, K., Gierz, P., et al. (2023). The impact of different atmospheric CO_2 concentrations on large scale Miocene temperature signatures. *Paleoceanography and Paleoclimatology*, *38*, e2022PA004438. https://doi.org/10.1029/2022PA004438

Received 23 FEB 2022
Accepted 12 JAN 2023
Corrected 10 FEB 2023

This article was corrected on 10 FEB 2023. See the end of the full text for details.

Author Contributions:

Conceptualization: Akil Hossain, Gregor Knorr, Wilfried Jokat, Gerrit Lohmann
Data curation: Akil Hossain, Katharina Hochmuth
Formal analysis: Akil Hossain, Gregor Knorr, Christian Stepanek

Abstract Based on inferences from proxy records the Miocene (23.03–5.33 Ma) was a time of amplified polar warmth compared to today. However, it remains a challenge to simulate a warm Miocene climate and pronounced polar warmth at reconstructed Miocene CO_2 concentrations. Using a state-of-the-art Earth-System-Model, we implement a high-resolution paleobathymetry and simulate Miocene climate at different atmospheric CO_2 concentrations. We estimate global mean surface warming of +3.1°C relative to the preindustrial at a CO_2 level of 450 ppm. An increase of atmospheric CO_2 from 280 to 450 ppm provides an individual warming of ∼1.4°C, which is as strong as all other Miocene forcing contributions combined. Substantial changes in surface albedo are vital to explain Miocene surface warming. Simulated surface temperatures fit well with proxy reconstructions at low- to mid-latitudes. The high latitude cooling bias becomes less pronounced for higher atmospheric CO_2 concentrations. At such CO_2 levels simulated Miocene climate shows a reduced polar amplification, linked to a breakdown of seasonality in the Arctic Ocean. A pronounced warming in boreal fall is detected for a CO_2 increase from 280 to 450 ppm, in comparison to weaker warming for CO_2 changes from 450 to 720 ppm. Moreover, a pronounced warming in winter is detected for a CO_2 increase from 450 to 720 ppm, in contrast to a moderate summer temperature increase, which is accompanied by a strong sea-ice concentration decline that promotes cloud formation in summer via enhanced moisture availability. As a consequence planetary albedo increases and dampens the temperature response to CO_2 forcing at a warmer Miocene background climate.

1. Introduction

Proxy reconstructions show that the Miocene was a time period of global warmth. During this time, the configuration of continents, oceans and main orographies were only moderately different from those at present. With moderately higher atmospheric CO_2 and higher temperatures, the Miocene Climatic Optimum (MCO; ∼16.9–14.7 Ma) has been suggested as a partial analog for the Earth's future greenhouse climate (Steinthorsdottir et al., 2021).

During the entire Miocene most proxy records reveal that atmospheric CO_2 was near or only moderately higher than preindustrial values (Beerling & Royer, 2011; Pagani et al., 2013; Sosdian et al., 2020; Steinthorsdottir et al., 2021; Super et al., 2018). Proxy reconstructions indicate that CO_2 concentrations were in the range of 300–600 ppm during the Miocene (Foster et al., 2017; Sosdian et al., 2018). For the MCO, a similar range of 400–600 ppm has been reported (Beerling et al., 2009; Kürschner et al., 2008; Royer, 2001; Steinthorsdottir et al., 2021). However, some reconstructions suggest that CO_2 levels may have been up to 1,137 ppm (Herbert et al., 2022; Rae et al., 2021; Sosdian et al., 2018; Stoll et al., 2019).

Previous modeling studies targeting the Early, Middle and Late Miocene using CO_2 concentrations of 200–850 ppm, modern orbital forcing, preindustrial aerosols, and taking reconstructed paleogeography, vegetation, and ice sheet differences into account, suggest a substantial high-latitude (>60°N and 60°S) warming (0–18°C in the Northern Hemisphere and 0–38°C in the Southern Hemisphere), while the temperature increase in the tropics (∼0–8°C) is less pronounced (Bradshaw et al., 2012, 2021; Burls et al., 2021; Farnsworth et al., 2019; Frigola et al., 2018; Herold, Huber, Greenwood, et al., 2011; Herold, Huber, & Müller, 2011, Herold et al., 2012; Knorr et al., 2011; Knorr & Lohmann, 2014; Stärz et al., 2017; Zhang et al., 2014). In these simulations the polar

Funding acquisition: Gregor Knorr, Wilfried Jokat, Gerrit Lohmann, Karsten Gohl
Investigation: Akil Hossain, Gregor Knorr, Christian Stepanek
Methodology: Akil Hossain, Gregor Knorr, Paul Gierz
Project Administration: Gregor Knorr, Wilfried Jokat, Gerrit Lohmann, Karsten Gohl
Software: Akil Hossain, Paul Gierz
Supervision: Gregor Knorr, Wilfried Jokat, Gerrit Lohmann
Validation: Akil Hossain
Visualization: Akil Hossain, Christian Stepanek
Writing – original draft: Akil Hossain
Writing – review & editing: Akil Hossain, Gregor Knorr, Wilfried Jokat, Gerrit Lohmann, Katharina Hochmuth, Karsten Gohl, Christian Stepanek

amplified warming is a robust feature and therefore the meridional temperature gradient is weaker during the Miocene than today (Burls et al., 2021). The wide range of temperature increase in the Southern Hemisphere reflects differences in Antarctic Ice Sheet configurations prescribed in these simulations.

Furthermore, several modeling studies have explored the role of different potential mechanisms on the climate of the Miocene. Global temperature and climatic changes are believed to have been primarily related to increased CO_2 concentrations, paleogeographic changes (including bathymetry, orography and ocean gateways; Hossain et al., 2020, 2021; Micheels et al., 2009; Mikolajewicz & Crowley, 1997; Von der Heydt & Dijkstra, 2006), changes in the vegetation (Bradshaw et al., 2015; Forrest et al., 2015; Knorr et al., 2011) and the sea ice-albedo feedback mechanism. The radiative forcing including prescribed atmospheric CO_2 concentration reveals a potentially dominant control on global-scale temperature changes (Steinthorsdottir et al., 2021). Miocene non-CO_2 boundary conditions such as paleogeography and ice sheets can raise the mean global temperature by ∼2°C (Burls et al., 2021). Higher atmospheric CO_2 and more effective ocean mixing could have contributed to a reduced summer-to-winter range of temperature (Lohmann et al., 2022; Spicer et al., 2004; Valdes et al., 1996). While these mechanisms have been identified to enable warmer temperatures in the models, it is still difficult to reconcile the Miocene polar amplified warmth observed in the proxy data with simulations (Burls et al., 2021; Steinthorsdottir et al., 2021).

Comparison of MPI-ESM Middle Miocene simulations with terrestrial proxies shows best agreement with simulations of 480 and 720 ppm CO_2, whereas the best agreement for marine proxies is detected at 360 and 480 ppm CO_2 (Krapp & Jungclaus, 2011). A different study using CCSM3 Middle Miocene simulations (conducted with 335 ppm CO_2 and comparing with terrestrial temperature records) shows +1.4°C warming in the model compared with +6°C in the proxies (Herold, Huber, & Müller, 2011). Goldner et al. (2014), using CESM1.0 simulations of the Middle Miocene with 400 ppm CO_2, find that global mean surface temperature is ∼4°C colder than indicated by the proxy reconstructions. The largest cold biases are in the mid- to high-latitudes, indicating a pronounced meridional temperature gradient of ∼17°C (Goldner et al., 2014; Herold, Huber, & Müller, 2011; Steinthorsdottir et al., 2021). Burls et al. (2021) assess the current range of model-data agreement and current advancement toward simulating Miocene warmth and demonstrate that the degree of weakening of the meridional temperature gradient and polar amplification increases with prescribed CO_2 forcing. A recent study (Lohmann et al., 2022) reveals that, global mean surface and meridional temperature characteristics similar to those found in MCO reconstructions may be obtained in climate simulations assuming relatively moderate CO_2 levels (450 ppm) with enhanced ocean mixing. The study finds a moderate low-latitude and pronounced high-latitude warming where substantial temperature increase by up to ∼5–10°C in surface temperature is widespread and Arctic temperature anomalies reach ∼12°C relative to preindustrial (Lohmann et al., 2022). However, it remains a major challenge to successfully simulate the Miocene high-latitudes climate with a fully coupled ocean-atmosphere model (Burls et al., 2021).

Using the proxy estimates of Miocene atmospheric CO_2 levels (300–600 ppm), no climate model experiment has so far reproduced the elevated proxy paleo temperatures (Burls et al., 2021; Steinthorsdottir et al., 2021) unless the effectivity of the ocean in transporting heat between low- and high latitudes on the one hand and surface and deep ocean on the other hand is enhanced, for example, via adaptation to the model's mixing parameterization (Lohmann et al., 2022). The model simulations cannot capture the full extent of the mid-latitude and polar warmth of the Miocene and do not have the skill to reproduce a reduced Miocene meridional temperature gradient (Burls et al., 2021; Goldner et al., 2014). It is obvious that our understanding of important physical parameters or positive feedbacks is incomplete to explain and describe processes that maintained the much weaker than preindustrial equator-to-pole temperature difference.

In this contribution we apply a state-of-the-art fully coupled Earth System Model to investigate the effect of newly and enhanced Miocene on-/offshore topographic information on the climate sensitivity at different atmospheric CO_2 concentrations. Our model is based on the work by Sidorenko et al. (2019) but considers vegetation dynamics. The model simulation uses a high-resolution global reconstruction of Miocene bathymetry and topography (Hochmuth, Gohl, et al., 2020; Paxman et al., 2019; Straume et al., 2020), which captures the major features of paleobathymetry (such as ocean ridges, plateaus and margins) and paleotopography (such as mountain ranges, e.g., the Andes). Reflecting the impact of many of these topographic features in climate simulations is only possible based on the flexibility of our ocean model with respect to spatial resolution that comes with the finite volume approach. Based on this novel setup, we investigate the climate impact of Miocene boundary conditions,

separating the effect of atmospheric CO_2 and non-CO_2 Miocene boundary conditions and quantifying the most important mechanisms/feedbacks that dominate temperature responses relative to the pre-industrial climate. The model simulations are evaluated with available proxy records of terrestrial and sea surface temperature (SST) reconstructions. In our model experiments, we examine the breakdown of seasonality in the Arctic Ocean with increasing CO_2 levels.

2. Materials and Methods

2.1. Model

We apply the AWI Earth System Model, version 2.1 (AWI-ESM2.1), which consists of the atmosphere general circulation model ECHAM6 (version 6.3.05p2; Stevens et al., 2013), the land-vegetation model JSBACH (Brovkin et al., 2009; Giorgetta et al., 2013; Raddatz et al., 2007; Reick et al., 2013) and the ocean model FESOM2 (Danilov et al., 2017; Scholz et al., 2019; Sidorenko et al., 2019). The coupling between ECHAM6 and FESOM2 is achieved via the OASIS3-MCT coupler (Valcke, 2013). AWI-ESM2.1 is derived from the AWI Climate Model, version 2 (AWI-CM2) that is based on the finite-volume formulation of FESOM2 (Danilov et al., 2017; Sidorenko et al., 2019). The ECHAM6 employs a spectral dynamical core and is used in our study at T63 resolution (∼1.88° × 1.88°; ∼180 km horizontal resolution at the equator) with 47 vertical layers. The land surface model JSBACH runs at the same horizontal resolution as ECHAM6. Spatial resolution in the ocean on the other hand is fundamentally different as FESOM2 employs, depending on the geographical setup, either the COREII mesh (∼127,000 nodes) or one of its paleo-derivates. The mesh resolution for FESOM2 is high in critical areas (up to ∼20 km) where small scale processes influence ocean dynamics.

AWI-ESM2.1 includes JSBACH with interactive vegetation dynamics, which ensures that climate-vegetation feedbacks are resolved in the model and that for any simulated climate state vegetation and climate are consistent with each other. Plant functional types are used in JSBACH to reduce the complexity that lies in the diversity of plants while still enabling differentiation of plant type's characteristics in the model. Our model setup considers thirteen plant functional types that describe various types of shrubs, grasses and trees. Vegetation types compete with each other and provide distinct properties for, among others, water carrying capacity and vegetation albedo (Groner et al., 2018), thus influencing both the water and energy balance in dependence of simulated vegetation distribution. Atmosphere-ocean coupling is performed in two steps. The ocean communicates its surface state to the atmosphere and is at the same time driven by atmospheric fluxes. Four ocean fields are sent to ECHAM6: sea ice concentration, sea ice thickness, SST, and snow on sea ice. ECHAM6 computes 12 air-sea fluxes (e.g., heat, momentum, freshwater fluxes) based on surface fields provided by FESOM2. So far, the AWI-ESM2 has not only been validated under modern climate conditions (Sidorenko et al., 2019) but also has been successfully applied for marine radiocarbon concentrations (Lohmann et al., 2020), the latest Holocene (Vorrath et al., 2020), the Last Interglacial (Otto-Bliesner et al., 2021) and the Last Glacial Maximum (Kageyama et al., 2021).

2.2. Paleobathymetry and Paleotopography

The paleomodel setup is based on the Middle Miocene time period (∼14 Ma) comprising the combined high-resolution (0.1° × 0.1°) global paleobathymetry and paleotopography of Straume et al. (2020), Hochmuth, Gohl, et al. (2020) and Paxman et al. (2019) (Figure 1). Paleobathymetry at latitudes south of 30°S is reconstructed following the paleobathymetric reconstruction of Hochmuth, Gohl, et al. (2020), using sediment backstripping (Steckler & Watts, 1978). It is based on the reconstruction by Straume et al. (2020) and includes a suite of new paleobathymetric grids of the Southern Ocean. Hochmuth, Paxman, et al. (2020) merged the Southern Ocean (Hochmuth, Gohl, et al., 2020) and Antarctic bathymetry/topography (Paxman et al., 2019). This Antarctic median topography is the most recent reconstruction with a resolution of approximately 5 km. The northern part (north of 30°S) of it uses the paleobathymetric reconstruction of Straume et al. (2020). The transition between the grids is smoothed to avoid artificial abrupt changes in the bathymetry.

Straume et al. (2020) have re-evaluated the evolution of the Northern Hemisphere oceanic gateways (i.e., Fram Strait, Greenland-Scotland Ridge, Central American Seaway, and Tethys Seaway) and embedded their tectonic histories in a new global paleobathymetry and paleotopography model. The model implements updated plate kinematics, oceanic lithospheric ages, estimated sediment thickness, and paleodepths of oceanic plateaus and microcontinents.

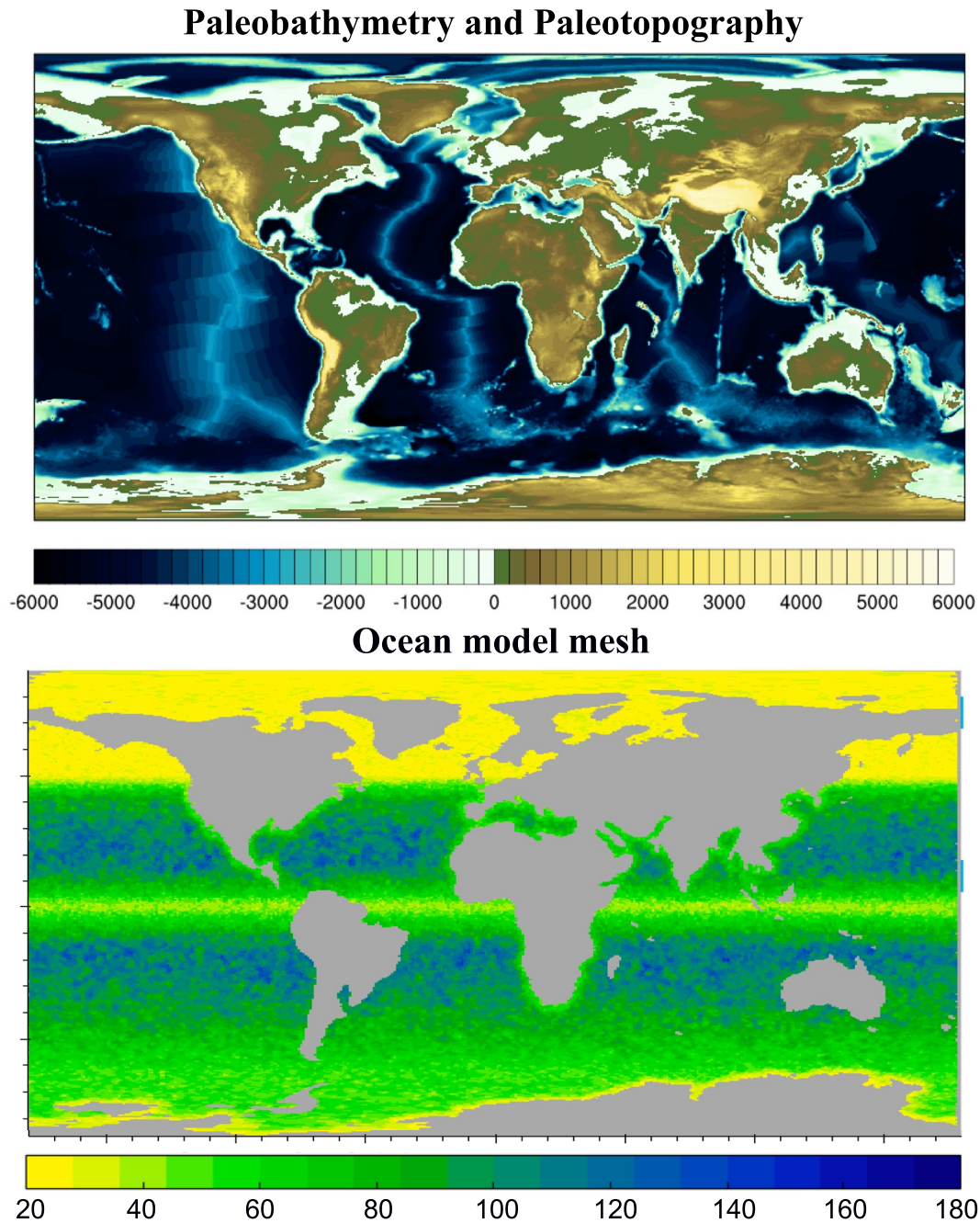

Figure 1. Global compilation of Middle Miocene paleobathymetry and paleotopography (in m) (Hochmuth, Gohl, et al., 2020; Paxman et al., 2019; Straume et al., 2020) and the ocean model mesh (in km).

2.3. Model Setup and Experimental Design

In our reference Miocene simulation (MIO_450) we prescribe an atmospheric CO_2 concentration of 450 ppm. We implement a high-resolution paleobathymetry and paleotopography of the Middle Miocene as described above. The Fram Strait represents a single ocean gateway control toward the Arctic Ocean (Butt et al., 2002). The North Atlantic gateways are wide enough to maintain rotationally controlled flows across the gateways and have geometries that are documented in Table 1 (in particular, Greenland-Scotland Ridge: depth: ~410 m; Fram Strait: depth: ~2,400 m, width: ~420 km). Other ocean gateways like the Canadian Archipelago, Bering Strait, Tethys Seaway, and similarly the Barents Sea, evolved after the Middle Miocene. Moreover, the Panama Seaway still connects the Pacific and Atlantic Oceans. In our Miocene setup the Greenland ice sheet is absent, whereas the height of the

Table 1
List of Sensitivity Experiments Including Relevant Model Parameters

Model exp.	Greenland-Scotland ridge depth (m)	Max. Fram depth (m)	Bathymetry and topography	Atmos. CO_2 (ppm)
MIO_280	~410	~2,400	Middle Miocene	280
MIO_450	~410	~2,400	Middle Miocene	450
MIO_720	~410	~2,400	Middle Miocene	720
PI_CTRL	~1,100	~2,800	Preindustrial	280
PI_450	~1,100	~2,800	Preindustrial	450

Antarctic ice sheets and the Miocene orography (East Africa, Andes, Rocky Mountains, Tibetan Plateau) are reduced compared to preindustrial. In our simulations orbital parameters are kept constant at preindustrial values. Similarly, we prescribe aerosols and atmospheric concentrations of greenhouse gases other than CO_2 (e.g., CH_4 and N_2O) to preindustrial levels. Distribution of vegetation in all simulations is computed by the model based on vegetation dynamics in JSBACH so that geographical coverage of plants varies based upon the climatic conditions (Figure S1 in Supporting Information S1).

To set up the Miocene simulations we first created an ocean mesh (Figure 1b) using the paleobathymetry and paleotopography (Hochmuth, Gohl, et al., 2020; Paxman et al., 2019; Straume et al., 2020). In order to create an initial spin-up of the ocean state FESOM2 was run in standalone mode for around 300 model years, initializing the ocean from a zero motion, constant temperature (3.5°C), constant salinity (34.7 psu) state. The coupled atmosphere-ocean model was then initialized from the standalone ocean spin up and integrated for 1,000 model years until a quasi-equilibrium state had been reached (Figure S2 in Supporting Information S1).

For reference, we also perform another AWI-ESM2.1 model simulation using an atmospheric CO_2 concentration of 280 ppm (PI_CTRL) and employing preindustrial boundary conditions (ocean bathymetry and topography, orbital forcing and ice sheet topography), vegetation again being adjusted dynamically based on the simulated climate state. This simulation has been initialized from three-dimensional preindustrial ocean salinity and temperature fields of the Polar Science Center Hydrographic Climatology (Steele et al., 2001).

In order to separate effects, and analyze relative importance of CO_2 forcing versus forcing by other boundary conditions, we present three additional simulations MIO_280, MIO_720 and PI_450 (Table 1). For simulation MIO_280 we apply the same CO_2 concentration as that used in PI_CTRL, but force the model with other boundary conditions as per Miocene. Simulation PI_450 adopts the same boundary conditions as PI_CTRL, while it is run with a higher CO_2 concentration of 450 ppm. In order to analyze the effect of boundary conditions, their complex interaction and synergy between them, we utilized a factor separation analysis (Stein & Alpert, 1993). Additionally, to investigate and disentangle dominant mechanisms that govern the global surface temperature changes in the high- and low-latitudes and shape Miocene climate, we employ both a zero-dimensional and one-dimensional energy balance model (Heinemann et al., 2009; Lunt et al., 2012). Further details of the energy balance model are given in Supporting Information S1 (Text S1).

Results of model simulations are compared to available reconstructions of surface temperature over land and ocean. We employ Middle Miocene terrestrial annual mean temperature estimates as collected and employed in MioMIP1 (Burls et al., 2021). We compare these estimates, that are derived mainly from fossil plant data, to the annual-mean land surface temperature of our simulations. In order to quantify the agreement of simulated and reconstructed Miocene SST we rely on temperature estimates as collected and employed in MioMIP1 (Burls et al., 2021) and as present from the Miocene temperature portal (Lawrence et al., 2021 and references therein). SST reconstructions employed in MioMIP1 are based on Mg/Ca, U^k_{37}, and TEX_{86} proxies, uncertainties are 3–5°C. Reconstructions of SST are representative of the Late Miocene (ranging between 11.6 and 5.33 Ma), Middle Miocene (ranging between 15.97 and 11.63 Ma) and MCO (ranging between 16.75 and 14.5 Ma). Information on all SST proxy records of Middle Miocene, MCO and Late Miocene considered in our study are, together with the original reference, provided in Tables S4 and S5 (extended version of the original table published in Burls et al. (2021)).

3. Results

3.1. Climatic Effect of Miocene Boundary Conditions

In experiment MIO_450 with Miocene boundary conditions, we simulate a mean surface air temperature (SAT) of ~16.4°C, which is warmer (~3.0°C) than the preindustrial climate (PI_CTRL, ~13.4°C). In comparison to the preindustrial the simulated Middle Miocene climate shows reduced sea-ice cover and increased water vapor (Figure 2 and Table 2). Spatial temperature anomaly patterns between MIO_450 and PI_CTRL are heterogeneous (Figure 2a). In combination with ice-albedo feedback (Figures 2b and 2c), the resulting temperature variation is largely pronounced in the high-latitudes.

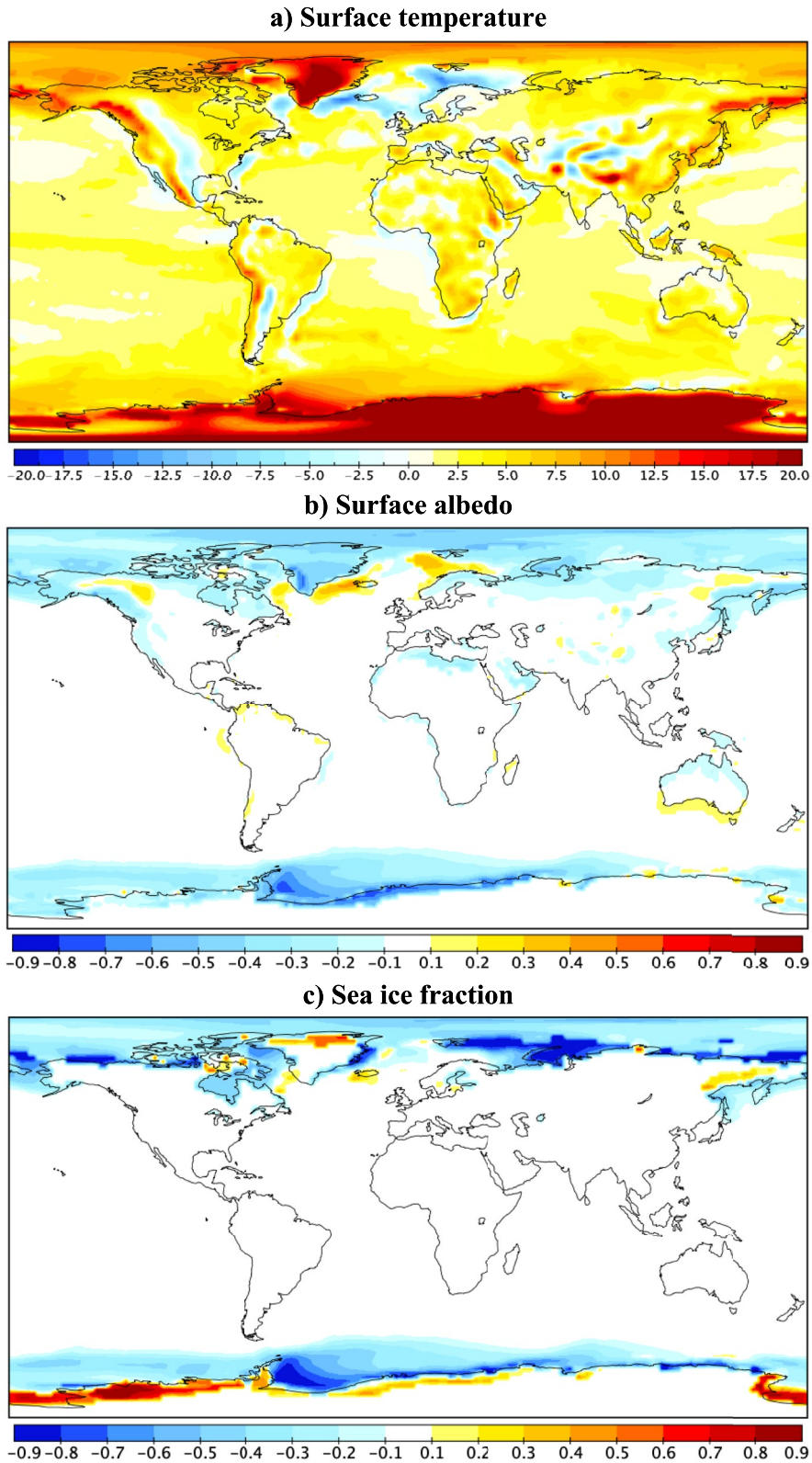

Figure 2. Annually averaged differences of (a) surface air temperature (SAT; in °C), (b) surface albedo and (c) sea ice fraction between the Middle Miocene (MIO_450) and the pre-industrial climate state (PI_CTRL).

Table 2
Key Diagnostics of Different Model Simulations

Model ex.	Mean SAT (°C)	Mean SST (°C)	Mean temperature at ~2,400 m	Mean SSS (psu)	Mean Arctic SAT (°C)	DJF mean Arctic SAT (°C)	MAM mean Arctic SAT (°C)	JJA mean Arctic SAT (°C)	SON mean Arctic SAT (°C)	Mean Arctic SST (°C)	Mean Arctic SSS (psu)	Equator to pole[a] temperature gradient (K)	Global mean vert. integr. water vapor (kg/m^2)
MIO_280	14.7	17.5	3.1	34.8	−15.2	−28.7	−18.4	−0.8	−12.5	−1.6	31.7	34.4	22.7
MIO_450	16.4	18.7	3.9	34.7	−9.8	−21.8	−13.8	−0.3	−3.6	−1.4	31.2	31.8	25.5
MIO_720	18.1	20.0	4.7	34.6	−5.1	−10.9	−9.5	0.7	−0.4	−0.7	30.8	29.4	28.9
PI_CTRL	13.3	16.6	1.8	34.6	−16.9	−33.1	−22.3	−1.6	−18.5	−1.8	32.8	34.6	21.4
PI_450	14.7	17.5	3.2	34.7	−12.8	−27.8	−17.4	−1.1	−11.6	−1.6	32.3	32.2	23.6

[a]Equator-to-pole temperature gradient for proxies is 24.5°C.

The most pronounced warming occurs over Antarctica, exceeding temperature anomalies of +35°C, and Greenland (+28°C). Other regions of exceptional warming are the Weddell Sea and Ross Sea, with a warming of up to +20°C. Furthermore, the warming at the western border of North and South America and across the Tibetan Plateau is mainly related to topography changes between Miocene and preindustrial simulation setups (Figure 2). The only region with a pronounced cooling is located in the Nordic Seas (e.g., by ~14°C), which is associated with a relatively shallow Greenland-Scotland Ridge in comparison to preindustrial (please see Section 3.2 for further details) and in combination with ice-albedo feedback (Figures 2b and 2c). Albedo changes at the continental boundaries are mostly controlled by displacement of the continents during the Miocene (Figure 1), contributing to the temperature changes in those regions (Figure 2).

3.2. Impact of Atmospheric CO_2 and Synergetic Effects

To evaluate the relative importance of CO_2 concentrations (ΔCO_2) and non-CO_2 Miocene boundary conditions (ΔBC) as forcing factors we used a factor separation analysis (Stein & Alpert, 1993). We compare our simulations PI_450 and MIO_280 with the preindustrial climate simulation (PI_CTRL). According to this analysis, the synergy ($\Delta Synergy$) is the difference of the combined boundary conditions effect ($\Delta(BC + CO_2)$) and the singular effects ΔBC and ΔCO_2 (Figure 3). The two simulations PI_450 and MIO_280 (Figures 3b and 3a) clearly show that changes in the CO_2 concentrations and non-CO_2 boundary conditions strongly alter the global temperature pattern. The global-mean surface temperature increase of ~3.1°C in MIO_450 can be attributed to the impact of the atmospheric CO_2 increase from 280 to 450 ppm ($\Delta CO_2 = +1.4$°C) and the effect of boundary conditions changes other than CO_2 ($\Delta BC = +1.4$°C), while the synergy between them is positive ($\Delta Synergy = +0.3$°C).

The resulting temperature increase is very pronounced over Antarctica (+30°C), Greenland (+22°C), Weddell Sea and Ross Sea, which is largely controlled by reduced ice sheet height and sea ice cover (SIC) during the Miocene. In contrast, a pronounced cooling occurs in the Nordic Seas and Barents Sea where temperature decreases by −16°C in combination with increased SIC and surface albedo (Figure 2). Temperature changes in this region are related to a Greenland-Scotland Ridge that is shallower than for the preindustrial (Hossain et al., 2020). The relatively shallow Greenland-Scotland Ridge reduces the transport of warmer and saltier Atlantic waters to the Nordic Seas. The reduced exchange of warm salty water across the gateway largely controls the overall temperature and salinity decrease (by up to −6 psu) at the ocean surface in the Nordic Seas and Barents Sea (Figure S3 in Supporting Information S1; Hossain et al., 2020).

The factor separation analysis indicates that warming over the Arctic and Southern Ocean (except for the regions of the Weddell Sea) can be attributed rather equally to both forcing factors (atmospheric CO_2 and non-CO_2 Miocene boundary conditions). The warming at the western border of North America, southern border of Siberia and Tibetan Plateau is related to displacement of the continents (between Miocene and preindustrial; Figure 3a), while the warming over all land masses is due to CO_2 changes (Figure 3b). The surface temperature changes in the Nordic Seas and Barents Sea are dominated by the associated bathymetry changes in these regions that predominantly have a cooling effect on climate.

The Labrador Sea and the North Atlantic (e.g., south of Iceland) are strongly influenced by the positive (i.e., warming) synergy between the non-CO_2 boundary conditions and the CO_2 forcing. In contrast to these

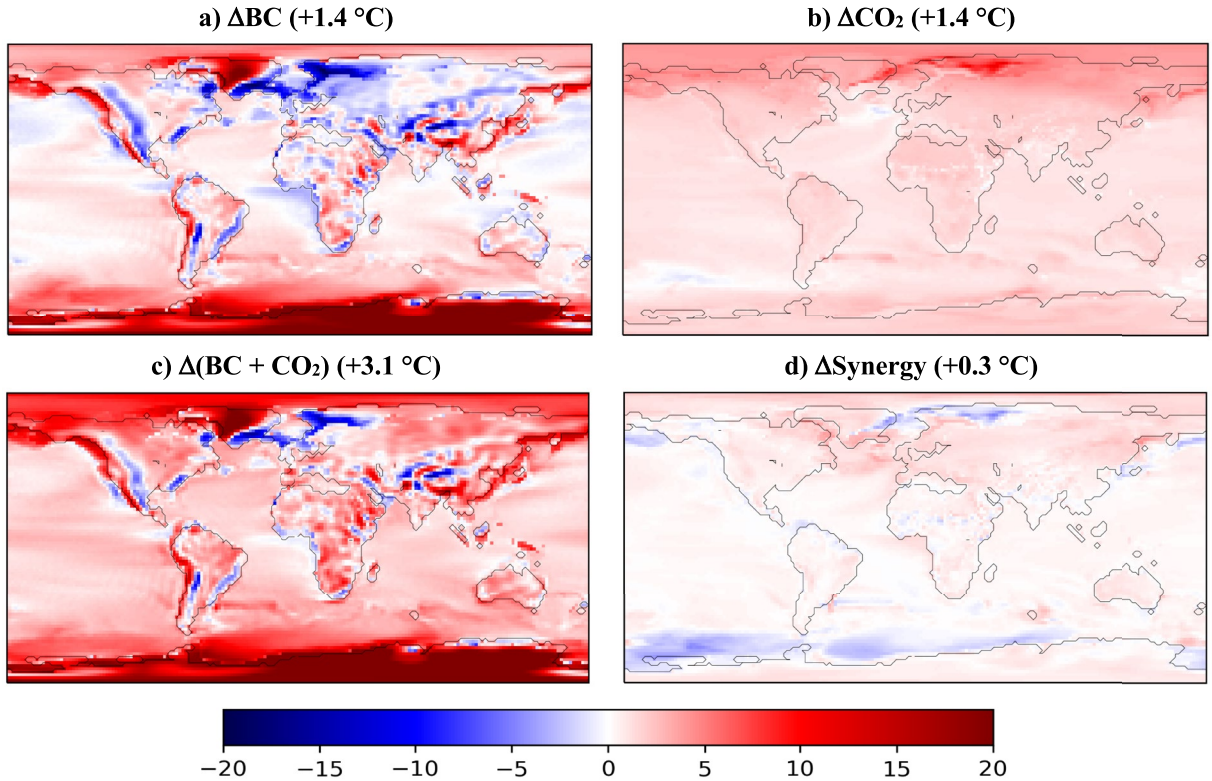

Figure 3. Application of a synergy analysis between non-CO_2 boundary conditions and atmospheric CO_2. Synergy analysis (ΔSynergy, (d) between (a) changing non-CO_2 Miocene boundary conditions (ΔBC), (b) changing CO_2 (ΔCO_2), and (c) the combined effect $\Delta(BC + CO_2)$ with respect to a change in the surface air temperature (SAT in °C).

regions the negative (i.e., cooling) synergy is pronounced over Nordic Seas and Barents Sea. At the southern high-latitudes, the negative synergy effect is pronounced in the Southern Ocean, particularly in the Weddell Sea, the Ross Sea and larger coastal region of the Antarctica (Figure 3). The enhanced synergy impact in these regions can be explained by high temperature sensitivity of sea-ice and associated feedbacks that are already triggered by global temperature change in ΔBC and ΔCO_2. Therefore, the combined effect of both forcing factors can cause a weaker warming at regional-scale, as well as an overall positive effect at the global-scale (Figure 3d).

To investigate the dominant mechanisms that govern global surface temperature differences in the high- and low-latitudes responses, we analyze a one-dimensional energy balance model for SAT, which shows a good agreement with the global mean SAT of the earth system model (Table S1 in Supporting Information S1). Deviations between the SAT as diagnosed by the one-dimensional energy balance model and the simulated climate are mainly occurring in the high latitudes (Figure 4a). The increase in zonal mean SAT, that comes with Miocene boundary conditions and increased CO_2, and that is biased toward the high latitudes, is associated with increased water vapor in the atmosphere, which reduces effective longwave emissivity (Figures 4b and 4d).

Our study suggests that substantial changes in surface albedo (Figure 4c) are vital to explain the Miocene surface warming (Figure 2). We compare the effective longwave emissivity and the planetary albedo of MIO_450 and PI_CTRL to quantify the impact on surface warming and to better explain the global radiation balance. The planetary albedo in MIO_450 is reduced by ∼0.01 (relative to PI_CTRL; 0.30), which causes less shortwave reflection, and, as a result, warming. The emissivity in MIO_450 also decreases by ∼0.02, which is largely governed by a ∼19% increase of the water vapor content in the atmosphere (Table 2) and enhances the greenhouse effect. Based on the energy balance model (Heinemann et al., 2009; Lunt et al., 2012) the impact of albedo and emissivity can be quantified (see e.g., Lohmann et al., 2022). About two-thirds (∼1.74 K) of the overall temperature anomaly with respect to PI_CTRL (∼2.60 K) are due to emissivity, whereas the remainder is due to reduced planetary albedo (Figure 4 and Table S1 in Supporting Information S1).

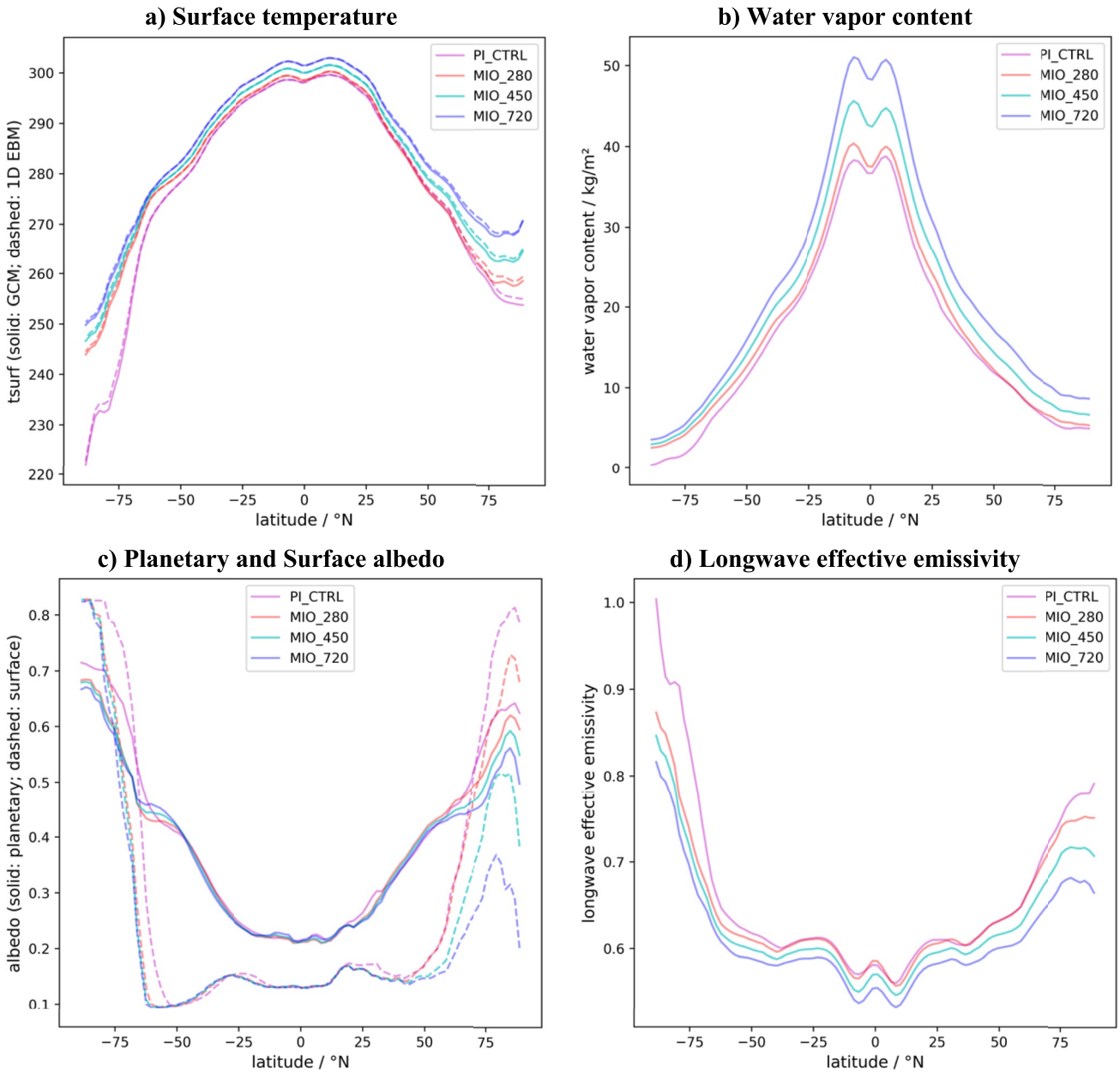

Figure 4. Meridional profile of contributors to temperature change in Miocene simulations. (a) Zonal mean profiles of the Miocene surface temperature (in K) as calculated by climate model (GCM; solid lines) and as diagnosed from one-dimensional (1D EBM) energy balance model (dashed lines); (b) vertically integrated water vapor content in the GCM; (c) surface albedo, simulated by the GCM (dashed), and planetary albedo, diagnosed from the 1D EBM (solid); (d) longwave effective emissivity diagnosed from the 1D EBM.

3.3. Data-Model Comparison

We compare the simulated annual-mean surface temperatures of land and ocean for Miocene experiments against available proxy data estimates of Middle Miocene, MCO and Late Miocene temperature proxy reconstructions (for details of the proxy compilation please see Tables S4 and S5; Burls et al., 2021; Lawrence et al., 2021 and references therein). Reconstructed temperatures are compared to zonal means of simulations and spatial patterns of simulated surface temperatures are shown in Figures 5 and 6 alongside a data set of Middle Miocene temperature proxy reconstructions (Burls et al., 2021; Lawrence et al., 2021). Both the terrestrial and SST proxies of the Middle Miocene indicate a reduced meridional temperature gradient while the model simulates a substantial meridional temperature gradient (Figures 5a and 5b). The model simulations appear to demonstrate

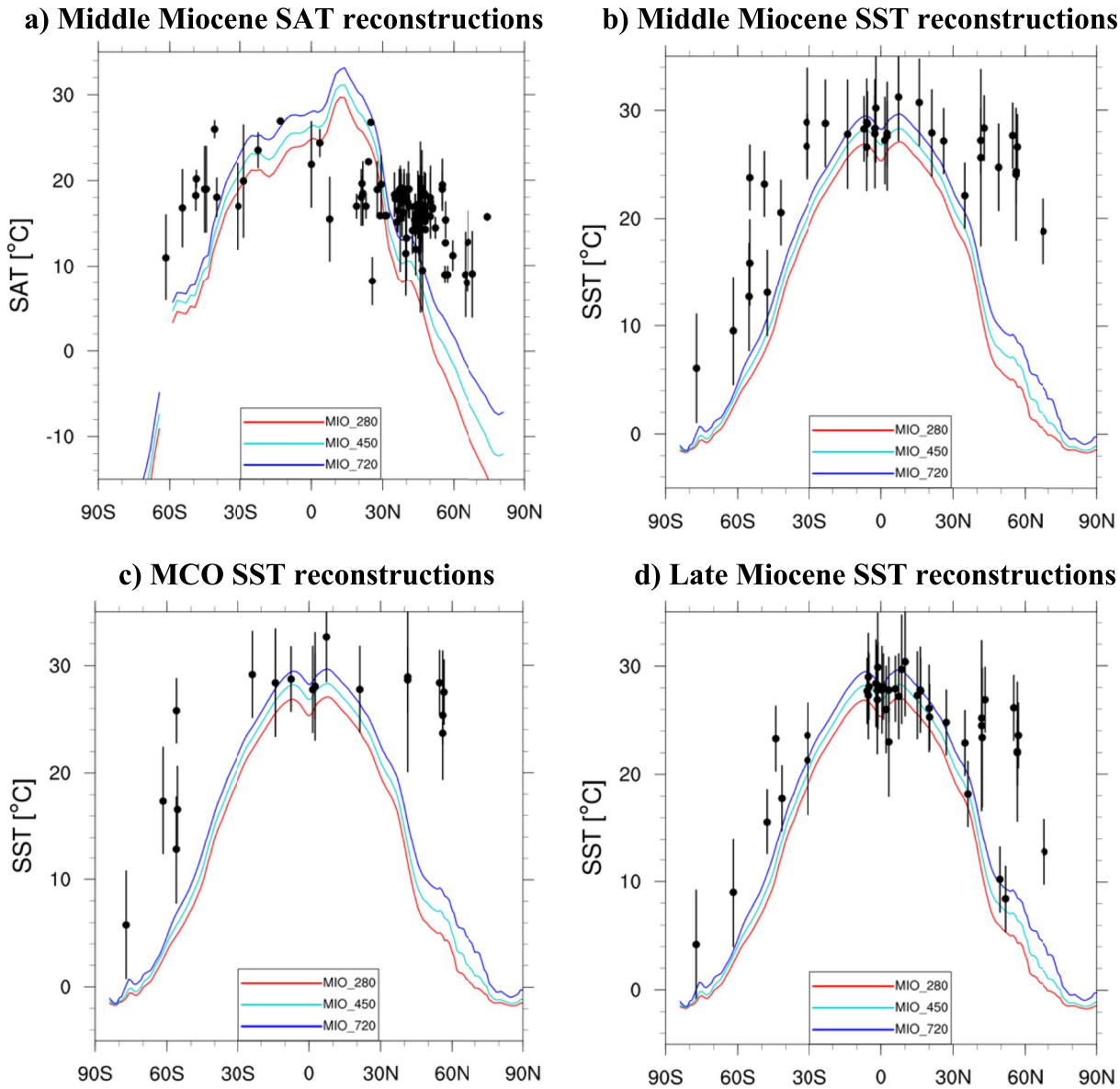

Figure 5. (a) Zonal-annual-mean surface air temperature (SAT; in °C) for all Miocene experiments. The circles localize Middle Miocene terrestrial temperature reconstructions (Burls et al., 2021). Zonal-annual-mean sea surface temperature (SST; in °C) for all Miocene experiments are shown in (b–d). The circles localize (b) Middle Miocene, (c) Miocene Climatic Optimum (MCO) and (d) Late Miocene sea surface temperature reconstructions (Table S5).

a reasonable fit with the low-latitude Middle Miocene SST records and the mid-latitude Middle Miocene SAT records (Figures 5b and 6). Simulations generally suffer from cold biases outside of the tropics. Modeled mid- to high-latitude warmth tends to show better agreement with the proxy data as CO_2 concentrations increase.

We detect cold SST biases in the Southern Ocean and the North Atlantic (Figure 6). In general, model simulations capture low to mid-latitude temperature distribution of the proxy data, but fail to capture the full extent of Miocene polar amplified warmth observed in the proxy records (Figures 5a and 5b). The nature of this mismatch can be explained by observing the equator-to-pole temperature gradient that is 4.9–9.9°C larger in the simulations than in the proxy reconstructions (Table 2). A reduction in modelled meridional temperature gradient is detected as CO_2 concentrations increase. Our simulations, MIO_450 and MIO_720 are roughly 5.8 ± 0.8°C and 4.5 ± 0.8°C colder compared to the SST calculated from the proxy records presented here (~24.5 ± 0.8°C; Burls et al., 2021). However, the model simulations show general agreement and a high and significant correlation coefficient with proxy data. The most significant correlation coefficient and lowest root-mean-square error (RMSE) with SST

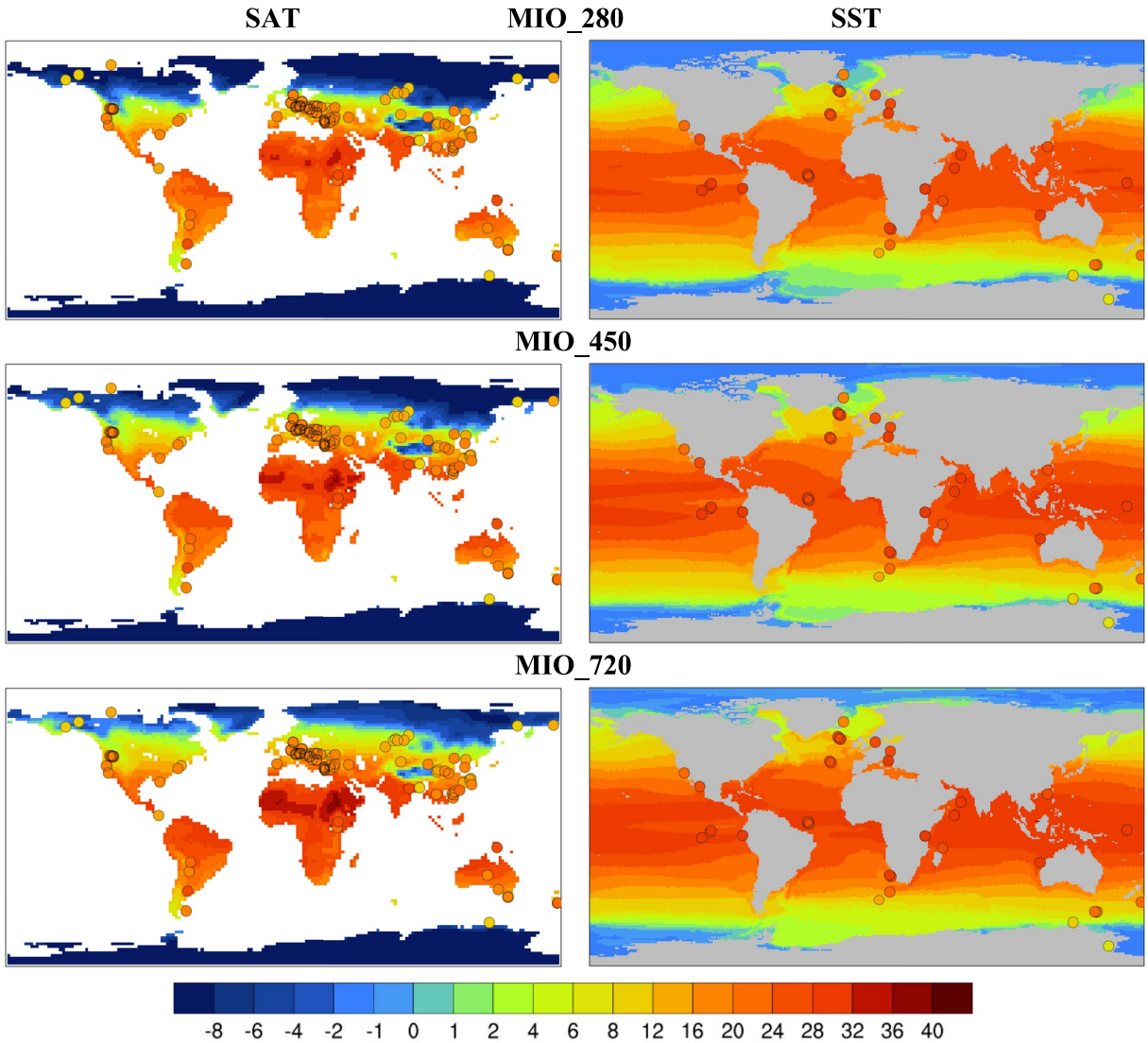

Figure 6. Global annual mean surface temperature of different Miocene experiments compared with the Middle Miocene mean annual surface air temperature (SAT; in °C) and sea surface temperature (SST; in °C) reconstructions. Background color fill: simulated global pattern of annual mean SAT and SST (in °C; left: SAT; right: SST). Colors of circles show the temperature as recorded by different proxy records, respectively.

records is detected for the Miocene simulation with 720 ppm of CO_2 ($R = 0.86$, RMSE = 7.1; Figure 7; Table S2 in Supporting Information S1). However, correlation coefficients of other simulations are very similar. Terrestrial temperature proxies also demonstrate the lowest RMSE with the MIO_720 simulation.

Deviation between model and reconstructions becomes larger when we consider the MCO SST proxies (Figure 5; Table S2 in Supporting Information S1). Our model simulations struggle to reproduce the elevated temperatures and reduced meridional temperature gradient estimated by the MCO SST proxies. In our experiments, the low-latitudes appear to provide a reasonable fit with Late Miocene proxies while mid- to high-latitudes are too cold (Figure 5 and Figure S4 in Supporting Information S1). We find most significant correlation coefficient and lowest deviations for the simulation with 720 ppm of CO_2 ($R = 0.90$, RMSE = 4.3; Table S2 in Supporting Information S1). Overall, we find that model simulations have better alignment with Late Miocene proxies than with reconstructions of Middle Miocene and MCO (Figure 7 and Figure S5 in Supporting Information S1) We note that the overall disagreement of simulated and reconstructed climate (i.e., a relatively cold climate state in the model) is evident in different regions, and in particular at the high latitudes (Figures 5 and 6). Furthermore, we remark that, despite the relatively long model integration, the overall energy balance of the Earth System is not yet in equilibrium, with the net energy flux into the Earth System being positive and increasing with the prescribed

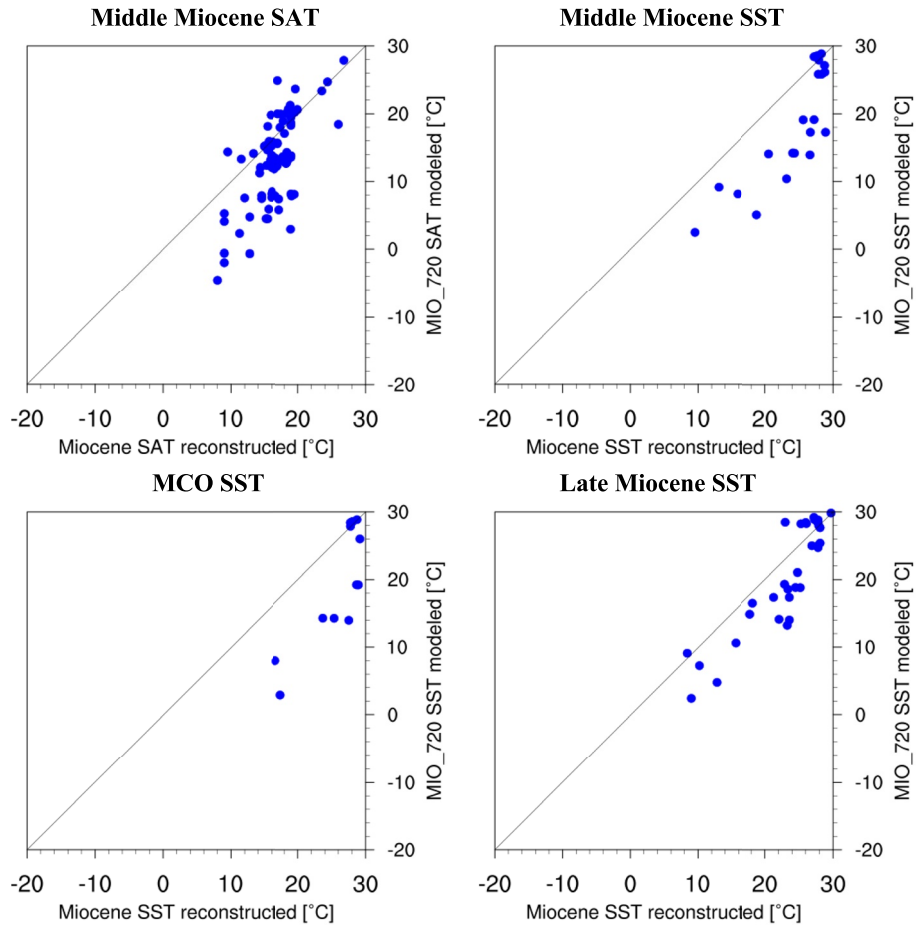

Figure 7. Comparison of reconstructed annual mean Miocene temperature changes versus Miocene experiment (that fits best with proxy reconstructions; MIO_720). All other cases are shown in Supporting Information S1 (Figure S5). The black line represents the 1:1 slope that indicates a perfect fit between reconstruction and simulation.

level of carbon dioxide (Table S1 in Supporting Information S1). We suggest that prolonged integration of the model could reduce the model data mismatch in particular in those regions where (polar) amplification of global warming is large (Figures 5 and 8), which have an overlap with regions of substantial model data mismatch.

3.4. Meridional Temperature Changes at Elevated CO_2 Concentration

Across the Miocene simulations (at different atmospheric CO_2 concentrations) the magnitude of high-latitude warming spans 10.2–13.3°C in the Southern Hemisphere and 1.7–11.8°C in the Northern Hemisphere compared to preindustrial, while low-latitude warming spans 0.6–3.4°C (Figure 8). We observe substantial polar amplified warmth in the high latitudes of both hemispheres across all Miocene simulations. In the higher northern latitudes, there is a pronounced polar amplification effect for CO_2 increase from 280 to 450 ppm (latitudinal mean surface temperature increase by ∼5.4°C; latitudes >80°N). The effect is weaker for the same radiative CO_2 forcing change from 450 to 720 ppm (latitudinal mean surface temperature increase by ∼4.7°C; latitudes >80°N) (Figure 8a). That means the impact of the CO_2 forcing is less pronounced at higher levels of CO_2 forcing. Temperature difference at low latitudes, is almost constant independent of the background level of CO_2.

Our warmest Miocene climate state with a CO_2 level of 720 ppm is characterized by a breakdown of seasonality in the Arctic Ocean. We detect a pronounced warming in boreal winter (December-January-February; DJF mean surface temperature increase by ∼10.9°C) for a CO_2 increase from 450 to 720 ppm, in contrast to a moderate boreal summer (June-July-August; JJA) temperature increase (mean surface temperature increase by ∼1.0°C; Figure 8 and Table 2). The change in the boreal summer temperature signature is accompanied by a strong sea-ice

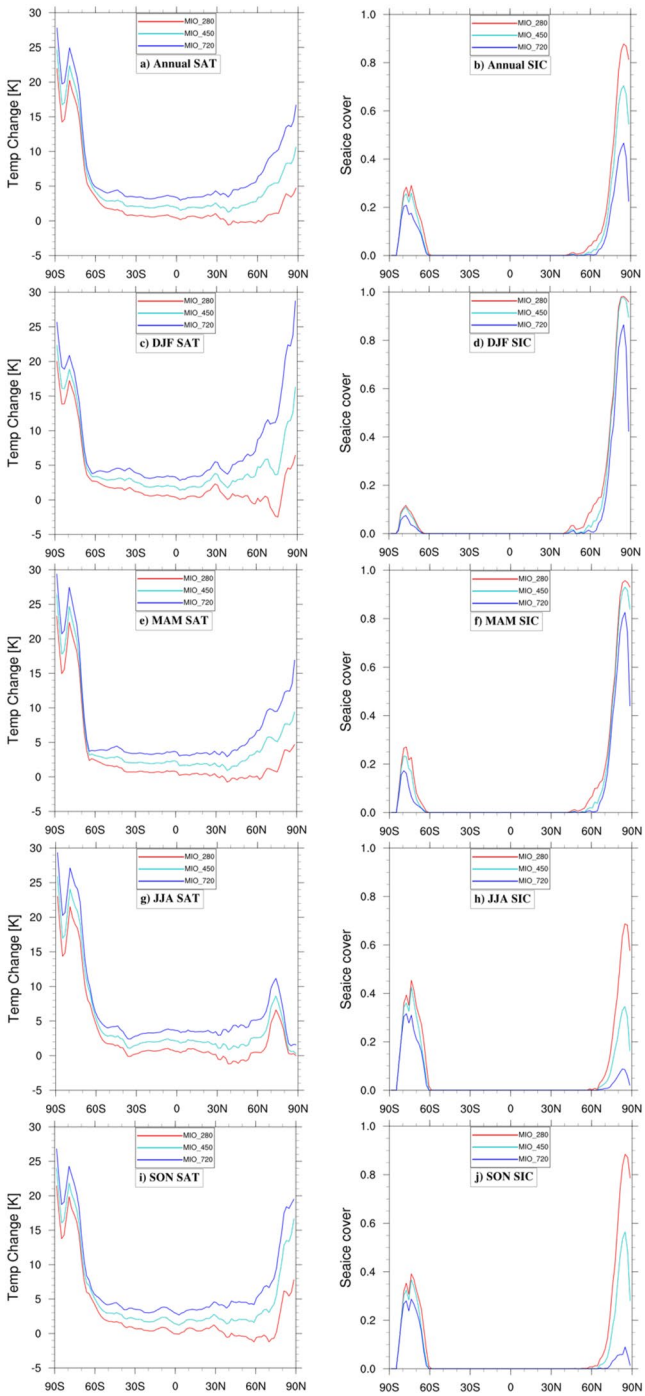

Figure 8. Zonal means of surface air temperature (SAT; left) and sea ice cover (SIC; right). Mean SAT change of Miocene experiments relative to the preindustrial state shown as (a) annual mean, (c) December-January-February (DJF), (e) March-April-May (MAM), (g) June-July-August (JJA) and (i) September-October-November (SON). Zonal mean SIC of Miocene experiments shown as (b) annual mean, (d) DJF, (f) MAM, (h) JJA and (j) SON.

concentration decline (Figure 8 and Figure S6 in Supporting Information S1) that promotes high-level cloud formation in the summer months via enhanced moisture availability (Figure 9 and Figures S7 and S8 in Supporting Information S1). As a consequence of enhanced cloud formation in the boreal summer months, the planetary albedo increases (Figure S9 in Supporting Information S1) which enhances reflection of solar radiation. It dampens the temperature response to the CO_2 forcing at a warmer Miocene background climate. In contrast, decreased sea ice extent and turbulent surface heat fluxes increase humidity in the lower atmosphere during boreal winter, which increases the low-level cloud cover (Figure S10 in Supporting Information S1). During polar night, this enhances downward longwave radiation, leading to a positive cloud-sea ice feedback. The heat released by the ocean and the cloud-sea ice feedback induce a pronounced warming in boreal winter (~22.2°C, relative to preindustrial; Table 2; Figure 9 and Figure S8 in Supporting Information S1). In addition, we detect a pronounced Arctic warming in boreal fall (September-October-November; SON) for a CO_2 increase from 280 to 450 ppm (mean surface temperature increase of ~8.9°C), in comparison to a weaker temperature increase for a CO_2 change from 450 to 720 ppm (mean surface temperature increase of ~3.2°C; Figure 8i and Table 2). The heat released by the ocean and the cloud feedbacks (high-level cloud cover is reduced, low-level cloud cover is increased) induce a pronounced warming in boreal fall for a CO_2 increase from 280 to 450 ppm (Table 2; Figure 9, Figures S7 and S10 in Supporting Information S1). The dampening of Arctic amplification to the same radiative forcing for a CO_2 change from 450 to 720 ppm is induced by moderate cloud feedbacks (Figures S7 and S10 in Supporting Information S1). Finally, we detect a similar moderate Arctic warming in boreal spring (March-April-May; MAM) for the same radiative CO_2 forcing changes from 280 to 450 ppm (mean surface warming of ~4.6°C) and 450–720 ppm (~4.3°C; Figure 8e).

4. Discussion

Findings derived from our climate simulations (Table 2) suggest a global annual average warming similar to previously published Middle Miocene climate simulations by Krapp and Jungclaus (2011), who found a global mean SAT of 17.1–19.2°C (at a CO_2 level of 480–720 ppm). Our simulated Miocene climate (based on CO_2 concentrations in the range of 280–720 ppm) shows a global mean SST of 17.5–20.0°C which is in good agreement with the Early to Middle Miocene simulations studied by Burls et al. (2021), but colder (3.7–6.7°C) than the global mean surface temperature estimates for the Middle Miocene (24.46°C ± 0.81°C) based on the compiled proxy SST synthesis (Burls et al., 2021). The modeled Miocene climate (MIO_450) exhibits a sensitive SAT response (+1.4°C) to CO_2 increase, which is governed by various climate feedbacks, such as water vapor (Soden & Held, 2006; +19% increase compared to preindustrial; Table 2) and sea-ice changes (Figure S6 in Supporting Information S1; Soden & Held, 2006; Knorr et al., 2011).

Non-CO_2 Miocene boundary conditions employed by us (including paleobathymetry and ice sheet height) raise global temperature by +1.4°C in agreement with previous estimates (Burls et al., 2021). Strong regional warming is detected in response to reduced height of the Antarctic ice sheet and absence of a Greenland ice sheet but the influence is limited beyond the high latitudes of both hemispheres (Burls et al., 2021). The largest contributor of warming relative to preindustrial (Figure 2) is caused by atmospheric CO_2 and land surface characteristics changes (e.g., surface albedo) that are linked with aspects of the global energy

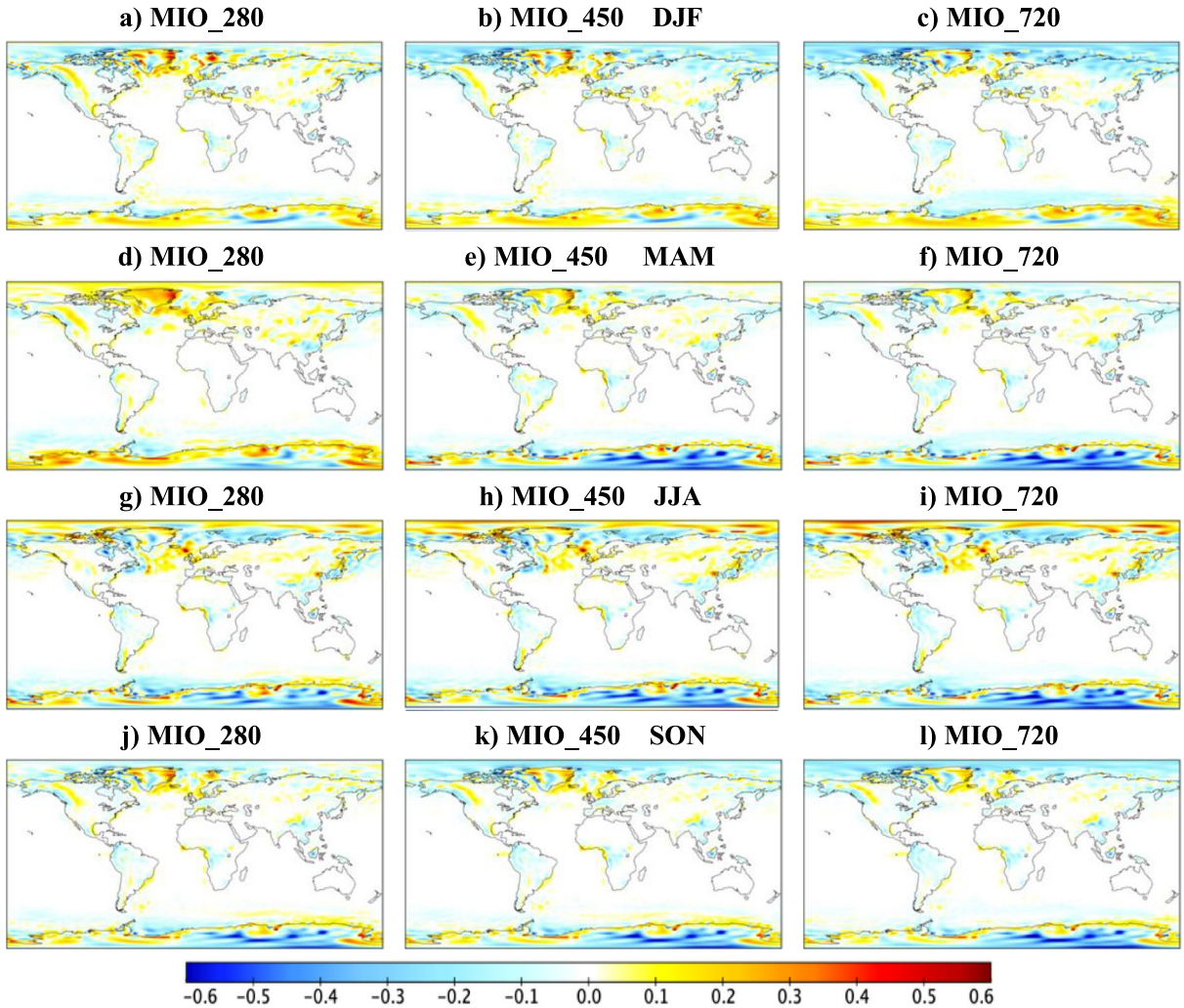

Figure 9. Global high-level cloud cover change of Middle Miocene experiments relative to the pre-industrial climate states (PI_CTRL) shown for (a–c) December-January-February (DJF), (d–f) March-April-May (MAM), (g–i) June-July-August (JJA) and (j–l) September-October-November (SON).

balance (e.g., effective longwave emissivity, planetary albedo; Figure 4; Burls et al., 2021; Knorr et al., 2011). Our climate simulations found a sea surface cooling in the Nordic Seas that is likely related to a relatively shallow Greenland-Scotland Ridge and the associated ice-albedo feedback, which is in agreement with the findings by Hossain et al. (2020).

During the MCO, different proxy reconstructions suggest that SSTs were 8–10°C warmer than preindustrial at high-latitudes of the Southern Hemisphere (Shevenell et al., 2004), 10–15°C warmer in the Northern Hemisphere (Super et al., 2020) and ~5–8°C warmer in the deep ocean (Lear et al., 2015), leading to a global mean surface warming of ~7.6 ± 2.3°C compared to preindustrial (Goldner et al., 2014). Results of our Miocene simulations are in agreement with this reconstructed range of temperature. The equator-to-pole gradient is 4.9–9.9°C larger in our simulations than that derived from proxy data (~17°C; Goldner et al., 2014). However, our Miocene climate simulations demonstrate a reasonable fit with low-latitude Middle Miocene SST and mid-latitude Middle Miocene SAT records. In general, the model simulations capture low- to mid-latitude temperature distributions of the proxy data. Both Middle Miocene terrestrial and SST proxies indicate a reduced meridional temperature gradient, while the model simulates a weakened, but in relation to reconstructions still pronounced meridional temperature gradient. The degree of weakening of the meridional temperature gradient and polar amplified warming increases in the simulations with prescribed CO_2 levels, but generally fails to capture the full extent of weakening of the reconstructed meridional temperature gradient observed in the proxies, a finding supported

by a previous study of Burls et al. (2021). It is noteworthy that our model simulations are not fully equilibrated, which leading the possibility that a part of the model data mismatch might be alleviated by further integration of the model (see Section 3.3).

The Miocene climate simulated by us is subject to weaker polar amplification at high northern latitudes (by 0.7°C) for CO_2 increase from 450 to 720 ppm relative to a similar change in radiative CO_2 forcing from 280 to 450 ppm (Figure 8). In polar regions, many feedback parameters are highly dependent on the presence of water in different phases and on the state of the system close to the freezing point (Goosse et al., 2018). Phase changes play a critical role in clouds of the polar region, leading to strong non-linearities in the cloud feedback (Mitchell et al., 1989; Zelinka et al., 2012). Moreover, as temperature increases, the surface area covered by ice or snow decreases at high-latitudes and the feedback strength is lowered (Goosse et al., 2018). Therefore, surface warming tends to be non-linear (deviation from the logarithmic curve) as CO_2 levels increase (Lunt et al., 2021), which supports our results.

Seasonal paleoclimate data suggest that polar amplification has a large seasonal cycle (Goosse et al., 2018; Utescher & Mosbrugger, 2007). The mean warming is at a minimum during boreal summer and maximum during boreal winter/fall with a peak in November in the Arctic Ocean (Laîné et al., 2016; Utescher & Mosbrugger, 2007). This result is again reproduced in our analysis of Miocene climate simulations. In a warmer climate, cloud cover increases (Figure S10 in Supporting Information S1), which increases the planetary albedo as well as the amount of reflected solar radiation. This process chain acts as a negative cloud optical depth feedback (Goosse et al., 2018). On the other hand, declining sea ice concentration during polar night (Figure 8) results in greater low-level clouds (Figure S10 in Supporting Information S1) and enhanced downwelling longwave radiation, leading to a positive cloud feedback. In boreal winter/fall, heat released by the ocean and cloud feedbacks induce a pronounced warming (Figures 8 and 9; Figure S8 in Supporting Information S1; Laîné et al., 2016; Goosse et al., 2018).

The inability of our model to capture the full extent of the reduction of meridional temperature gradient and polar amplified warmth reflected in proxies is an issue that is not only unique to either our model or to climate simulations of the Miocene epoch, but also seen in different paleoclimate modeling studies spanning the Cenozoic (Burls et al., 2021; Goldner et al., 2014; Haywood et al., 2020; Huber & Caballero, 2011; Krapp & Jungclaus, 2011; Steinthorsdottir et al., 2021). It is likely that our interpretation or understanding of proxy data signals is limited (Ho & Laepple, 2016) and our knowledge of important physical parameters or positive feedbacks is missing or incomplete to explain how climatic processes and trends are related to reconstructed temperature changes. However, implementation of enhanced ocean mixing (Lohmann et al., 2022), state-of-the-art parameterizations of cloud-aerosol interactions (Feng et al., 2019; Kiehl & Shields, 2013; Lunt et al., 2021; Zhu et al., 2019; Zhu & Poulsen, 2019) and improved representation of tidal mixing (Green & Huber, 2013; Lohmann, 2020) might improve the ability of models to simulate Miocene warmth and to reduce disagreement between modeled and reconstructed meridional temperature gradients. Model simulations with elevated CO_2 concentration, up to 1,100 ppm as recently reconstructed for the Early-Middle Miocene including the MCO by Herbert et al. (2022), might also provide a better fit between climate simulations and reconstructed temperatures.

5. Conclusions

By means of the state-of-the-art climate model AWI-ESM2.1, we have simulated Miocene climate states at different atmospheric CO_2 concentrations and evaluated the effect of model boundary conditions during the Middle Miocene. We estimate a global mean surface warming of +3.1°C relative to the preindustrial state at a CO_2 level of 450 ppm. The atmospheric CO_2 increase from 280 to 450 ppm provides an individual warming contribution of ∼1.4°C, which is as strong as all non-CO_2 Miocene forcing contributions combined (∼1.4°C). In combination with ice-albedo feedbacks, the resulting temperature change is largely pronounced at high-latitudes. A substantial cooling appears in the Nordic Seas which is associated with a relatively shallow Greenland-Scotland Ridge in comparison to modern bathymetry and in combination with ice-albedo changes. Our simulated surface temperatures fit well with proxy reconstructions except in the high-latitudes. Incomplete model equilibration may provide a partial explanation for this finding. The high-latitude cooling bias is least pronounced in our simulation with a CO_2 concentration of 720 ppm. The most significant correlation coefficient and lowest RMSE with terrestrial and SST records are detected for the simulation with the highest CO_2 level. Our climate simulation with a CO_2 level of 720 ppm shows reduced polar amplification, since the warmest Miocene climate state is

characterized by a breakdown of seasonality in the Arctic Ocean. We detect a pronounced warming in boreal fall for a CO_2 increase from 280 to 450 ppm, in comparison to a weaker warming for the same radiative CO_2 forcing changes from 450 to 720 ppm. This change in temperature sensitivity to the same radiative forcing is induced by more pronounced cloud feedbacks in the forcing window from 280 to 450 ppm. Moreover, a pronounced warming in boreal winter is detected for the simulations with higher CO_2 levels, which is in contrast to a moderate boreal summer warming response. The change in the seasonal temperature response is accompanied by a strong sea-ice concentration decline. Enhanced moisture availability promotes cloud formation during the summer months. As a consequence, planetary albedo increases (i.e., the reflection of solar radiation is enhanced) and dampens the temperature response to the CO_2 forcing in a warmer Miocene background climate.

Overall, our model simulations show general agreement and a significant correlation coefficient with proxy data and are in the range of other published Early to Middle Miocene simulations. Future sensitivity studies can use our model setup and evaluate the effect of high-resolution global paleobathymetry (implemented in our study) in combination with plausible mechanisms, that have been suggested to reduce model-reconstruction mismatches, on ocean circulation and climate. Promising candidates, that might be required for providing more realistic climatic response for the Miocene, are sensitivity studies with enhanced vertical mixing in the ocean (Lohmann et al., 2022), state-of-the-art parameterizations of cloud-aerosol interactions (Lunt et al., 2021; Zhu & Poulsen, 2019; Zhu et al., 2019), changes in aerosols (Lunt et al., 2021), as well as improved representation of tidal mixing (Green & Huber, 2013; Lohmann, 2020).

Conflict of Interest

The authors declare no conflicts of interest relevant to this study.

Data Availability Statement

Data from this study is available for further use through PANGAEA (Hossain et al., 2022). *Code availability*: The standard source code of the FESOM2 (Finite Element Sea ice-Ocean Model) is available to the public via GitHub (https://github.com/FESOM/fesom2/). The ECHAM6 model is available upon request from the Max Planck Institute (MPI) for Meteorology in Hamburg (https://mpimet.mpg.de/en/science/modeling-with-icon/code-avilability).

Acknowledgments
This study is supported through institutional funds of the Alfred Wegener Institute (AWI)—Helmholtz Centre for Polar and Marine Research through Work Packages 3.2 (Earth system on tectonic time scales: From greenhouse to icehouse world) and the topic "Ocean and Cryosphere under climate change" of its research program PACES-II "Changing Earth—Sustaining our Future" and the joint program "Changing Earth—Sustaining our Future" (PoF IV) program of the AWI. All simulations were performed at the AWI Computing Center. Thanks go to the scientific community in DeepMIP and MioMIP for their efforts toward provision of robust paleogeography and model forcing. The authors thank three anonymous reviews and editor for constructive comments that helped improving the manuscript. Open Access funding enabled and organized by Projekt DEAL.

References

Beerling, D. J., Fox, A., & Anderson, C. W. (2009). Quantitative uncertainty analyses of ancient atmospheric CO_2 estimates from fossil leaves. *American Journal of Science*, *309*(9), 775–787. https://doi.org/10.2475/09.2009.01

Beerling, D. J., & Royer, D. L. (2011). Convergent Cenozoic CO_2 history. *Nature Geoscience*, *4*(7), 418–420. https://doi.org/10.1038/ngeo1186

Bradshaw, C. D., Langebroek, P. M., Lear, C. H., Lunt, D. J., Coxall, H. K., Sosdian, S. M., & de Boer, A. M. (2021). Hydrological impact of Middle Miocene Antarctic ice-free areas coupled to deep ocean temperatures. *Nature Geoscience*, *14*(6), 429–436. https://doi.org/10.1038/s41561-021-00745-w

Bradshaw, C. D., Lunt, D., Flecker, R., Salzmann, U., Pound, M., Haywood, A., & Eronen, J. (2012). The relative roles of CO_2 and palaeogeography in determining late Miocene climate: Results from a terrestrial model-data comparison. *Climate of the Past*, *8*(2), 715–786. https://doi.org/10.5194/cp-8-1257-2012

Bradshaw, C. D., Lunt, D. J., Flecker, R., & Davies-Barnard, T. (2015). Disentangling the roles of late Miocene paleogeography and vegetation– implications for climate sensitivity. *Palaeogeography, Palaeoclimatology, Palaeoecology*, *417*, 17–34. https://doi.org/10.1016/j.palaeo.2014.10.003

Brovkin, V., Raddatz, T., Reick, C. H., Claussen, M., & Gayler, V. (2009). Global biogeophysical interactions between forest and climate. *Geophysical Research Letters*, *36*(7). https://doi.org/10.1029/2009gl037543

Burls, N. J., Bradshaw, C. D., De Boer, A. M., Herold, N., Huber, M., Pound, M., et al. (2021). *Simulating Miocene warmth: Insights from an opportunistic multi-model ensemble (MioMIP1)*. Paleoceanography and Paleoclimatology.

Butt, F. A., Drange, H., Elverhøi, A., Otterå, O. H., & Solheim, A. (2002). Modelling Late Cenozoic isostatic elevation changes in the Barents Sea and their implications for oceanic and climatic regimes: Preliminary results. *Quaternary Science Reviews*, *21*(14–15), 1643–1660. https://doi.org/10.1016/S0277-3791(02)00018-5

Danilov, S., Sidorenko, D., Wang, Q., & Jung, T. (2017). *The finite-volume sea ice–ocean model (FESOM2)* (Vol. 10, pp. 765–789). Geoscientific Model Development.

Farnsworth, A., Lunt, D. J., O'Brien, C. L., Foster, G. L., Inglis, G. N., Markwick, P., et al. (2019). Climate sensitivity on geological timescales controlled by nonlinear feedbacks and ocean circulation. *Geophysical Research Letters*, *46*(16), 9880–9889. https://doi.org/10.1029/2019gl083574

Feng, R., Otto-Bliesner, B. L., Xu, Y., Brady, E., Fletcher, T., & Ballantyne, A. (2019). Contributions of aerosol-cloud interactions to mid-Piacenzian seasonally sea ice-free Arctic Ocean. *Geophysical Research Letters*, *46*(16), 9920–9929. https://doi.org/10.1029/2019gl083960

Forrest, M., Eronen, J. T., Utescher, T., Knorr, G., Stepanek, C., Lohmann, G., & Hickler, T. (2015). Climate-vegetation modelling and fossil plant data suggest low atmospheric CO_2 in the late Miocene. *Climate of the Past*, *11*(12), 1701–1732. https://doi.org/10.5194/cp-11-1701-2015

Foster, G. L., Royer, D. L., & Lunt, D. J. (2017). Future climate forcing potentially without precedent in the last 420 million years. *Nature Communications*, *8*(1). https://doi.org/10.1038/ncomms14845

Frigola, A., Prange, M., & Schulz, M. (2018). Boundary conditions for the middle Miocene climate transition (MMCT v1.0). *Geoscientific Model Development*, *11*(4), 1607–1626. https://doi.org/10.5194/gmd-11-1607-2018

Giorgetta, M. A., Jungclaus, J., Reick, C. H., Legutke, S., Bader, J., Böttinger, M., et al. (2013). Climate and carbon cycle changes from 1850 to 2100 in MPI-ESM simulations for the Coupled Model Intercomparison Project phase 5. *Journal of Advances in Modeling Earth Systems*, *5*(3), 572–597. https://doi.org/10.1002/jame.20038

Goldner, A., Herold, N., & Huber, M. (2014). The challenge of simulating the warmth of the mid-Miocene climatic optimum in CESM1. *Climate of the Past*, *10*(2), 523–536. https://doi.org/10.5194/cp-10-523-2014

Goosse, H., Kay, J. E., Armour, K. C., Bodas-Salcedo, A., Chepfer, H., Docquier, D., et al. (2018). Quantifying climate feedbacks in polar regions. *Nature Communications*, *9*(1), 1–13. https://doi.org/10.1038/s41467-018-04173-0

Green, J. A. M., & Huber, M. (2013). Tidal dissipation in the early Eocene and implications for ocean mixing. *Geophysical Research Letters*, *40*(11), 2707–2713. https://doi.org/10.1002/grl.50510

Groner, V. P., Raddatz, T., Reick, C. H., & Claussen, M. (2018). Plant functional diversity affects climate–vegetation interaction. *Biogeosciences*, *15*(7), 1947–1968. https://doi.org/10.5194/bg-15-1947-2018

Haywood, A. M., Tindall, J. C., Dowsett, H. J., Dolan, A. M., Foley, K. M., Hunter, S. J., et al. (2020). A return to large-scale features of Pliocene climate: The Pliocene model intercomparison Project phase 2. *Climate of the Past Discussions*, *16*, 2095–2123. https://doi.org/10.5194/cp-2019-145

Heinemann, M., Jungclaus, J. H., & Marotzke, J. (2009). Warm Paleocene/Eocene climate as simulated in ECHAM5/MPIOM. *Climate of the Past*, *5*(4), 785–802. https://doi.org/10.5194/cp-5-785-2009

Herbert, T. D., Dalton, C. A., Liu, Z., Salazar, A., Si, W., & Wilson, D. S. (2022). Tectonic degassing drove global temperature trends since 20 Ma. *Science*, *377*(6601), 116–119. https://doi.org/10.1126/science.abl4353

Herold, N., Huber, M., Greenwood, D. R., Müller, R. D., & Seton, M. (2011). Early to middle Miocene monsoon climate in Australia. *Geology*, *39*(1), 3–6. https://doi.org/10.1130/G31208.1

Herold, N., Huber, M., & Müller, R. D. (2011). Modeling the Miocene climatic optimum. Part I: Land and atmosphere. *Journal of Climate*, *24*, 6353–6372. https://doi.org/10.1175/2011JCLI4035.1

Herold, N., Huber, M., Müller, R. D., & Seton, M. (2012). Modeling the Miocene climatic optimum: Ocean circulation. *Paleoceanography*, *27*(1), PA1209. https://doi.org/10.1029/2010PA002041

Ho, S. L., & Laepple, T. (2016). Flat meridional temperature gradient in the early Eocene in the subsurface rather than surface ocean. *Nature Geoscience*, *9*(8), 606–610. https://doi.org/10.1038/ngeo2763

Hochmuth, K., Gohl, K., Leitchenkov, G., Sauermilch, I., Whittaker, J. M., Uenzelmann-Neben, G., et al. (2020). The evolving paleobathymetry of the Circum-Antarctic Southern Ocean since 34 Ma: A key to understanding past cryosphere-ocean developments. *Geochemistry, Geophysics, Geosystems*, *21*(8), e2020GC009122. https://doi.org/10.1029/2020gc009122

Hochmuth, K., Paxman, G. J. G., Gohl, K., Jamieson, S. S. R., Leitchenkov, G. L., Bentley, M. J., et al. (2020). *Combined palaeotopography and palaeobathymetry of the Antarctic continent and the Southern Ocean since 34 Ma*. PANGAEA. Retrieved from https://doi.pangaea.de/10.1594/PANGAEA.923109

Hossain, A., Knorr, G., Jokat, W., & Lohmann, G. (2021). Opening of the Fram Strait led to the establishment of a modern-like three-layer stratification in the Arctic Ocean during the Miocene. *Arktos*, *7*(1–3), 1–12. https://doi.org/10.1007/s41063-020-00079-8

Hossain, A., Knorr, G., Jokat, W., Lohmann, G., Hochmuth, K., Gierz, P., & Gohl, K. (2022). Climate model results of different Miocene and Preindustrial atmospheric CO_2 concentrations experiments of AWI-ESM2 in NetCDF format [Dataset]. PANGAEA. https://doi.org/10.1594/PANGAEA.943430

Hossain, A., Knorr, G., Lohmann, G., Stärz, M., & Jokat, W. (2020). Simulated thermohaline fingerprints in response to different Greenland-Scotland ridge and Fram strait subsidence histories. *Paleoceanography and Paleoclimatology*, *35*(7), e2019PA003842. https://doi.org/10.1029/2019PA003842

Huber, M., & Caballero, R. (2011). The early Eocene equable climate problem revisited. *Climate of the Past*, *7*(2), 603–633. https://doi.org/10.5194/cp-7-603-2011

Kageyama, M., Harrison, S. P., Kapsch, M.-L., Lofverstrom, M., Lora, J. M., Mikolajewicz, U., et al. (2021). The PMIP4 Last Glacial Maximum experiments: Preliminary results and comparison with the PMIP3 simulations. *Climate of the Past*, *17*(3), 1065–1089. https://doi.org/10.5194/cp-17-1065-2021

Kiehl, J. T., & Shields, C. A. (2013). Sensitivity of the Palaeocene-Eocene thermal maximum climate to cloud properties. *Philosophical Transactions of the Royal Society A: Mathematical, Physical & Engineering Sciences*, *371*(2001), 20130093. https://doi.org/10.1098/rsta.2013.0093

Knorr, G., Butzin, M., Micheels, A., & Lohmann, G. (2011). A warm Miocene climate at low atmospheric CO_2 levels. *Geophysical Research Letters*, *38*(20), L20701. https://doi.org/10.1029/2011GL048873

Knorr, G., & Lohmann, G. (2014). Climate warming during Antarctic ice sheet expansion at the Middle Miocene transition. *Nature Geoscience*, *7*(5), 376–381. https://doi.org/10.1038/ngeo2119

Krapp, M., & Jungclaus, J. H. (2011). The middle Miocene climate as modeled in an atmosphere-ocean-biosphere model. *Climate of the Past*, *7*(4), 1169–1188. https://doi.org/10.5194/cp-7-1169-2011

Kürschner, W. M., Kvaček, Z., & Dilcher, D. L. (2008). The impact of Miocene atmospheric carbon dioxide fluctuations on climate and the evolution of terrestrial ecosystems. *Proceedings of the National Academy of Sciences of the United States of America*, *105*(2), 449–453. https://doi.org/10.1073/pnas.0708588105

Laîné, A., Yoshimori, M., & Abe-Ouchi, A. (2016). Surface Arctic amplification factors in CMIP5 models: Land and oceanic surfaces and seasonality. *Journal of Climate*, *29*(9), 3297–3316. https://doi.org/10.1175/jcli-d-15-0497.1

Lawrence, K., Coxall, H., Sosdian, S., & Steinthorsdottir, M. (2021). *Miocene temperature portal. Dataset version 2*. Bolin Centre Database. https://doi.org/10.17043/miocene-temperature-portal-2

Lear, C. H., Coxall, H. K., Foster, G. L., Lunt, D. J., Mawbey, E. M., Rosenthal, Y., et al. (2015). Neogene ice volume and ocean temperatures: Insights from infaunal foraminiferal Mg/Ca paleothermometry. *Paleoceanography*, *30*(11), 1437–1454. https://doi.org/10.1002/2015pa002833

Lohmann, G. (2020). Temperatures from energy balance models: The effective heat capacity matters. *Earth System Dynamics*, *11*(4), 1195–1208. https://doi.org/10.5194/esd-11-1195-2020

Lohmann, G., Butzin, M., Eissner, N., Shi, X., & Stepanek, C. (2020). Abrupt climate and weather changes across time scales. *Paleoceanography and Paleoclimatology*, *35*(9), e2019PA003782. https://doi.org/10.1029/2019PA003782

Lohmann, G., Knorr, G., Hossain, A., & Stepanek, C. (2022). Effects of CO_2 and ocean mixing on Miocene and Pliocene temperature gradients. *Paleoceanography and Paleoclimatology*, *35*(7), e2020PA003953. https://doi.org/10.1029/2020PA003953

Lunt, D. J., Bragg, F., Chan, W.-L., Hutchinson, D. K., Ladant, J.-B., Morozova, P., et al. (2021). DeepMIP: Model intercomparison of early Eocene climatic optimum (EECO) large-scale climate features and comparison with proxy data. *Climate of the Past*, *17*(1), 203–227. https://doi.org/10.5194/cp-17-203-2021

Lunt, D. J., Haywood, A. M., Schmidt, G. A., Salzmann, U., Valdes, P. J., Dowsett, H. J., & Loptson, C. A. (2012). On the causes of mid-Pliocene warmth and polar amplification. *Earth and Planetary Science Letters*, *321–322*, 128–138. https://doi.org/10.1016/j.epsl.2011.12.042

Micheels, A., Bruch, A. A., & Mosbrugger, V. (2009). Miocene climate modelling sensitivity experiments for different CO_2 concentrations. *Palaeontologia Electronica*, *12*, 1–20.

Mikolajewicz, U., & Crowley, T. J. (1997). Response of a coupled ocean/energy balance model to restricted flow through the Central American Isthmus. *Paleoceanography*, *12*(3), 429–441. https://doi.org/10.1029/96PA03542

Mitchell, J. F., Senior, C. A., & Ingram, W. J. (1989). CO_2 and climate: A missing feedback? *Nature*, *341*(6238), 132–134. https://doi.org/10.1038/341132a0

Otto-Bliesner, B. L., Brady, E. C., Zhao, A., Brierley, C. M., Axford, Y., Capron, E., et al. (2021). Large-scale features of Last interglacial climate: Results from evaluating the lig127k simulations for the coupled model intercomparison Project (CMIP6)–Paleoclimate Modeling Intercomparison Project (PMIP4). *Climate of the Past*, *17*(1), 63–94. https://doi.org/10.5194/cp-17-63-2021

Pagani, M., Huber, M., Liu, Z., Bohaty, S. M., Henderiks, J., Sijp, W., et al. (2013). The role of carbon dioxide during the onset of Antarctic glaciation. *Science*, *334*(6060), 1261–1264. https://doi.org/10.1126/science.1203909

Paxman, G. J. G., Jamieson, S. S. R., Hochmuth, K., Gohl, K., Bentley, M. J., Leitchenkov, G., & Ferraccioli, F. (2019). Reconstructions of Antarctic topography since the Eocene–Oligocene boundary. *Palaeogeography, Palaeoclimatology, Palaeoecology*, *535*, 109346. https://doi.org/10.1016/j.palaeo.2019.109346

Raddatz, T. J., Reick, C. H., Knorr, W., Kattge, J., Roeckner, E., Schnur, R., et al. (2007). Will the tropical land biosphere dominate the climate–carbon cycle feedback during the twenty-first century? *Climate Dynamics*, *29*(6), 565–574. https://doi.org/10.1007/s00382-007-0247-8

Rae, J. W., Zhang, Y. G., Liu, X., Foster, G. L., Stoll, H. M., & Whiteford, R. D. (2021). Atmospheric CO_2 over the past 66 million years from marine archives. *Annual Review of Earth and Planetary Sciences*, *49*(1), 609–641. https://doi.org/10.1146/annurev-earth-082420-063026

Reick, C. H., Raddatz, T., Brovkin, V., & Gayler, V. (2013). Representation of natural and anthropogenic land cover change in MPI-ESM. *Journal of Advances in Modeling Earth Systems*, *5*(3), 459–482. https://doi.org/10.1002/jame.20022

Royer, D. L. (2001). Stomatal density and stomatal index as indicators of paleoatmospheric CO_2 concentration. *Review of Palaeobotany and Palynology*, *114*(1–2), 1–28. https://doi.org/10.1016/S0034-6667(00)00074-9

Scholz, P., Sidorenko, D., Gurses, O., Danilov, S., Koldunov, N., Wang, Q., et al. (2019). Assessment of the finite VolumE Sea Ice Ocean Model (FESOM2.0), Part I: Description of selected key model elements and comparison to its predecessor version. *Geoscientific Model Development Discussions*, 1–42. https://doi.org/10.5194/gmd-2018-329

Shevenell, A. E., Kennett, J. P., & Lea, D. W. (2004). Middle Miocene Southern Ocean cooling and Antarctic cryosphere expansion. *Science*, *305*(5691), 1766–1770. https://doi.org/10.1126/science.1100061

Sidorenko, D., Goessling, H. F., Koldunov, N., Scholz, P., Danilov, S., Barbi, D., et al. (2019). Evaluation of FESOM2.0 coupled to ECHAM6.3: Preindustrial and HighResMIP simulations. *Journal of Advances in Modeling Earth Systems*, *11*, 3794–3815. https://doi.org/10.1029/2019ms001696

Soden, B. J., & Held, I. M. (2006). An assessment of climate feedbacks in coupled ocean-atmosphere models. *Journal of Climate*, *19*(14), 3354–3360. https://doi.org/10.1175/jcli3799.1

Sosdian, S. M., Babila, T. L., Greenop, R., Foster, G. L., & Lear, C. H. (2020). Ocean carbon storage across the middle Miocene: A new interpretation for the Monterey event. *Nature Communications*, *11*(1), 134. https://doi.org/10.1038/s41467-019-13792-0

Sosdian, S. M., Greenop, R., Hain, M. P., Foster, G. L., Pearson, P. N., & Lear, C. H. (2018). Constraining the evolution of Neogene ocean carbonate chemistry using the boron isotope pH proxy. *Earth and Planetary Science Letters*, *498*, 362–376. https://doi.org/10.1016/j.epsl.2018.06.017

Spicer, R. A., Herman, A. B., & Kennedy, E. M. (2004). The foliar physiognomicrecord of climatic conditions during dormancy: CLAMP and the cold monthmean temperature. *The Journal of Geology*, *112*(6), 685–702. https://doi.org/10.1086/424579

Stärz, M., Jokat, W., Knorr, G., & Lohmann, G. (2017). Threshold in north Atlantic-Arctic ocean circulation controlled by the subsidence of the Greenland-Scotland Ridge. *Nature Communications*, *8*(1), 15681. https://doi.org/10.1038/ncomms15681

Steckler, M. S., & Watts, A. B. (1978). Subsidence of the Atlantic-type continental margin off New York. *Earth and Planetary Science Letters*, *41*(1), 1–13. https://doi.org/10.1016/0012-821x(78)90036-5

Steele, M., Morley, R., & Ermold, W. (2001). PHC: A global ocean hydrography with a high-quality Arctic Ocean. *Journal of Climate*, *14*(9), 2079–2087. https://doi.org/10.1175/1520-0442(2001)014<2079:PAGOHW>2.0.CO;2

Stein, U., & Alpert, P. I. N. H. A. S. (1993). Factor separation in numerical simulations. *Journal of the Atmospheric Sciences*, *50*(14), 2107–2115. https://doi.org/10.1175/1520-0469(1993)050<2107:FSINS>2.0.CO;2

Steinthorsdottir, M., Coxall, H. K., De Boer, A. M., Huber, M., Barbolini, N., Bradshaw, C. D., et al. (2021). The Miocene: The future of the past. *Paleoceanography and Paleoclimatology*, *36*(4), e2020PA004037. https://doi.org/10.1029/2020pa004037

Stevens, B., Giorgetta, M., Esch, M., Mauritsen, T., Crueger, T., Rast, S., et al. (2013). Atmospheric component of the MPI-M Earth system model: ECHAM6. *Journal of Advances in Modeling Earth Systems*, *5*(2), 146–172. https://doi.org/10.1002/jame.20015

Stoll, H. M., Guitian, J., Hernandez-Almeida, I., Mejia, L. M., Phelps, S., Polissar, P., et al. (2019). Upregulation of phytoplankton carbon concentrating mechanisms during low CO_2 glacial periods and implications for the phytoplankton pCO_2 proxy. *Quaternary Science Reviews*, *208*, 1–20. https://doi.org/10.1016/j.quascirev.2019.01.012

Straume, E. O., Gaina, C., Medvedev, S., & Nisancioglu, K. H. (2020). Global Cenozoic paleobathymetry with a focus on the northern hemisphere oceanic gateways. *Gondwana Research*, *86*, 126–143. https://doi.org/10.1016/j.gr.2020.05.011

Super, J. R., Thomas, E., Pagani, M., Huber, M., O'Brien, C., & Hull, P. M. (2018). North Atlantic temperature and pCO_2 coupling in the early-middle Miocene. *Geology*, *46*(6), 519–522. https://doi.org/10.1130/G40228.1

Super, J. R., Thomas, E., Pagani, M., Huber, M., O'Brien, C. L., & Hull, P. M. (2020). Miocene evolution of North Atlantic sea surface temperature. *Paleoceanography and Paleoclimatology*, *35*(5), e2019PA003748. https://doi.org/10.1029/2019PA003748

Utescher, T., & Mosbrugger, V. (2007). Eocene vegetation patterns reconstructed from plant diversity—A global perspective. *Palaeogeography, Palaeoclimatology, Palaeoecology*, *247*(3–4), 243–271. https://doi.org/10.1016/j.palaeo.2006.10.022

Valcke, S. (2013). The OASIS3 coupler: A European climate modelling community software. *Geoscientific Model Development*, *6*(2), 373–388. https://doi.org/10.5194/gmd-6-373-2013

Valdes, P. J., Sellwood, B. W., & Price, G. D. (1996). The concept of Cretaceous equability. *Palaeoclimates Data and Modelling*, *1*, 139–158.

Von der Heydt, A., & Dijkstra, H. A. (2006). Effect of ocean gateways on the global ocean circulation in the late Oligocene and early Miocene. *Paleoceanography*, *21*(1), PA1011. https://doi.org/10.1029/2005PA001149

Vorrath, M.-E., Müller, J., Rebolledo, L., Cárdenas, P., Shi, X., Esper, O., et al. (2020). Sea ice dynamics in the Bransfield strait, Antarctic Peninsula, during the past 240 years: A multi-proxy intercomparison study. *Climate of the Past*, *16*(6), 2459–2483. https://doi.org/10.5194/cp-16-2459-2020

Zelinka, M. D., Klein, S. A., & Hartmann, D. L. (2012). Computing and partitioning cloud feedbacks using cloud property histograms. Part II: Attribution to changes in cloud amount, altitude, and optical depth. *Journal of Climate*, *25*(11), 3736–3754. https://doi.org/10.1175/jcli-d-11-00249.1

Zhang, Z., Ramstein, G., Schuster, M., Li, C., Contoux, C., & Yan, Q. (2014). Aridification of the Sahara desert caused by Tethys sea shrinkage during the late Miocene. *Nature*, *513*(7518), 401–404. https://doi.org/10.1038/nature13705

Zhu, J., & Poulsen, C. J. (2019). Quantifying the cloud particle-size feedback in an Earth System Model. *Geophysical Research Letters*, *46*(19), 10910–10917. https://doi.org/10.1029/2019GL083829

Zhu, J., Poulsen, C. J., & Tierney, J. E. (2019). Simulation of Eocene extreme warmth and high climate sensitivity through cloud feedbacks. *Science Advances*, *5*(9), eaax1874. https://doi.org/10.1126/sciadv.aax1874

References From the Supporting Information

Drury, A. J., & John, C. M. (2016). Exploring the potential of clumped isotope thermometry on coccolith-rich sediments as a sea surface temperature proxy. *PANGAEA*. https://doi.org/10.1594/PANGAEA.865019

Drury, A. J., Lee, G. P., Gray, W. R., Lyle, M., Westerhold, T., Shevenell, A. E., & John, C. M. (2018). Deciphering the State of the Late Miocene to Early Pliocene Equatorial Pacific. *Paleoceanography and Paleoclimatology*, *33*(3), 246–263. https://doi.org/10.1002/2017pa003245

Ehlers, B.-M., & Jokat, W. (2013). Paleo-bathymetry of the northern North Atlantic and consequences for the opening of the Fram Strait. *Marine Geophysical Research*, *34*(1), 25–43. https://doi.org/10.1007/s11001-013-9165-9

Emeis, K.-C., Schulz, H., Struck, U., Rossignol-Strick, M., Erlenkeuser, H., Howell, M. W., et al. (2003). Eastern Mediterranean surface water temperatures and δ18O composition during deposition of sapropels in the late quaternary. *Paleoceanography*, *18*(1). https://doi.org/10.1029/2000pa000617

Emeis, K.-C., Struck, U., Schulz, H.-M., Rosenberg, R., Bernasconi, S., Erlenkeuser, H., et al. (2000). Temperature and salinity variations of Mediterranean Sea surface waters over the last 16,000 years from records of planktonic stable oxygen isotopes and alkenone unsaturation ratios. *Palaeogeography, Palaeoclimatology, Palaeoecology*, *158*(3–4), 259–280. https://doi.org/10.1016/s0031-0182(00)00053-5

Fox, L. R., Wade, B. S., Holbourn, A., Leng, M. J., & Bhatia, R. (2021). Temperature gradients across the Pacific Ocean during the middle Miocene. *Paleoceanography and Paleoclimatology*, *36*(6). https://doi.org/10.1029/2020pa003924

Guitián, J., Phelps, S., Polissar, P. J., Ausín, B., Eglinton, T. I., & Stoll, H. M. (2019). Midlatitude temperature variations in the Oligocene to early Miocene. *Paleoceanography and Paleoclimatology*, *34*(8), 1328–1343. https://doi.org/10.1029/2019pa003638

Hall, R. (2012). Sundaland and Wallacea: Geology, plate tectonics and palaeogeography. In D. J. Gower, J. E. Richardson, B. R. Rosen, L. Rueber, & S. T. Williams (Eds.), *Biotic evolution and environmental change in Southeast Asia* (pp. 32–78). Cambridge University Press.

Herbert, T. D., Peterson, L. C., Lawrence, K. T., & Liu, Z. (2010). Tropical ocean temperatures over the past 3.5 million years. *Science*, *328*(5985), 1530–1534. https://doi.org/10.1126/science.1185435

Herbert, T. D., Ng, G., & Cleaveland Peterson, L. (2015). Evolution of Mediterranean Sea surface temperatures 3.5−1.5 Ma: Regional and hemispheric influences. *Earth and Planetary Science Letters*, *409*, 307–318. https://doi.org/10.1016/j.epsl.2014.10.006

Herbert, T. D., Lawrence, K. T., Tzanova, A., Peterson, L. C., Caballero-Gill, R., & Kelly, C. S. (2016). Late Miocene global cooling and the rise of modern ecosystems. *Nature Geoscience*, *9*(11), 843–847. https://doi.org/10.1038/ngeo2813

Herbert, T. D., Rose, R., Dybkjær, K., Rasmussen, E. S., & Śliwińska, K. K. (2020). Bihemispheric warming in the Miocene climatic optimum as seen from the Danish North Sea. *Paleoceanography and Paleoclimatology*, *35*(10), e2020PA003935. https://doi.org/10.1029/2020pa003935

Holbourn, A., Kuhnt, W., Regenberg, M., Schulz, M., Mix, A., & Andersen, N. (2010). Does Antarctic glaciation force migration of the tropical rain belt? *Geology*, *38*(9), 783–786. https://doi.org/10.1130/g31043.1

Holbourn, A. E., Kuhnt, W., Clemens, S. C., Kochhann, K. G. D., Jöhnck, J., Lübbers, J., & Andersen, N. (2018). Late Miocene climate cooling and intensification of southeast Asian winter monsoon. *Nature Communications*, *9*(1), 1584. https://doi.org/10.1038/s41467-018-03950-1

Huang, Y., Clemens, S. C., Liu, W., Wang, Y., & Prell, W. L. (2007). Large-scale hydrological change drove the late Miocene C4 plant expansion in the Himalayan foreland and Arabian Peninsula. *Geology*, *35*(6), 531. https://doi.org/10.1130/g23666a.1

Kuhnert, H., Bickert, T., & Paulsen, H. (2009). Southern Ocean frontal system changes precede Antarctic ice sheet growth during the middle Miocene. *Earth and Planetary Science Letters*, *284*(3–4), 630–638. https://doi.org/10.1016/j.epsl.2009.05.030

LaRiviere, J. P., Ravelo, A. C., Crimmins, A., Dekens, P. S., Ford, H. L., Lyle, M., & Wara, M. W. (2012). Late Miocene decoupling of oceanic warmth and atmospheric carbon dioxide forcing. *Nature*, *486*(7401), 97–100. https://doi.org/10.1038/nature11200

Lawrence, K. T., Herbert, T. D., Brown, C. M., Raymo, M. E., & Haywood, A. M. (2009). High-amplitude variations in North Atlantic sea surface temperature during the early Pliocene warm period. *Paleoceanography*, *24*(2). https://doi.org/10.1029/2008pa001669

Lawrence, K. T., Liu, Z., & Herbert, T. D. (2006). Evolution of the eastern tropical Pacific through Plio-Pleistocene glaciation. *Science*, *312*(5770), 79–83. https://doi.org/10.1126/science.1120395

Leutert, T. J., Auderset, A., Martínez-García, A., Modestou, S., & Meckler, A. N. (2020). Temperatures from TEX86 measurements performed on middle Miocene sediment material from ODP Hole 189-1171C [Dataset]. PANGAEA. https://doi.org/10.1594/PANGAEA.919351

Levy, R., Harwood, D., Florindo, F., Sangiorgi, F., Tripati, R., von Eynatten, H., et al. (2016). Antarctic ice sheet sensitivity to atmospheric CO_2 variations in the early to mid-Miocene. *Proceedings of the National Academy of Sciences*, *113*(13), 3453–3458. https://doi.org/10.1073/pnas.1516030113

Liu, J., Tian, J., Liu, Z., Herbert, T. D., Fedorov, A. V., & Lyle, M. (2019). Eastern equatorial Pacific cold tongue evolution since the late Miocene linked to extratropical climate. *Science Advances*, *5*(4). https://doi.org/10.1126/sciadv.aau6060

Liu, Z., & Herbert, T. D. (2004). High-latitude influence on the eastern equatorial Pacific climate in the early Pleistocene epoch. *Nature*, *427*(6976), 720–723. https://doi.org/10.1038/nature02338

Montes, C., Cardona, A., McFadden, R., Moron, S. E., Silva, C. A., Restrepo-Moreno, S., et al. (2012). Evidence for middle Eocene and younger land emergence in central Panama: Implications for Isthmus closure. *The Geological Society of America Bulletin*, *124*(5–6), 780–799. https://doi.org/10.1130/b30528.1

Morley, R. J. (2011). *Cretaceous and Tertiary climate change and the past distribution of megathermal rainforests*. In M. Bush, J. Flenley, & W. Gosling (Eds.), (pp. 1–34). Springer Praxis Books.

Nairn, M., Lear, C., Sosdian, S., Bailey, T., & Beavington-Penney, S. (2021). Tropical Sea surface temperatures following the middle Miocene climate transition from Laser-Ablation ICP-MS analysis of glassy foraminifera. *Zenodo*. https://doi.org/10.5281/ZENODO.4472994

Nathan, S. A., & Leckie, R. M. (2009). Early history of the Western Pacific Warm Pool during the middle to late Miocene (~13.2–5.8 Ma): Role of sea-level change and implications for equatorial circulation. *Palaeogeography, Palaeoclimatology, Palaeoecology*, *274*(3–4), 140–159. https://doi.org/10.1016/j.palaeo.2009.01.007

Pound, M. J., Haywood, A. M., Salzmann, U., & Riding, J. B. (2012). Global vegetation dynamics and latitudinal temperature gradients during the Mid to Late Miocene (15.97–5.33 Ma). *Earth-Science Reviews*, *112*(1–2), 22. https://doi.org/10.1016/j.earscirev.2012.02.005

Rommerskirchen, F., Condon, T., Mollenhauer, G., Dupont, L., & Schefuss, E. (2011). Miocene to Pliocene development of surface and subsurface temperatures in the Benguela Current system. *Paleoceanography*, *26*(3). https://doi.org/10.1029/2010pa002074

Rousselle, G., Beltran, C., Sicre, M.-A., Raffi, I., & De Rafélis, M. (2013). Changes in sea-surface conditions in the Equatorial Pacific during the middle Miocene–Pliocene as inferred from coccolith geochemistry. *Earth and Planetary Science Letters*, *361*, 412–421. https://doi.org/10.1016/j.epsl.2012.11.003

Sangiorgi, F., Bijl, P. K., Passchier, S., Salzmann, U., Schouten, S., McKay, R., et al. (2018). Southern Ocean warming and Wilkes Land ice sheet retreat during the mid-Miocene. *Nature Communications*, *9*(1), 317. https://doi.org/10.1038/s41467-017-02609-7

Sangiorgi, F., Quaijtaal, W., Donders, T. H., Schouten, S., & Louwye, S. (2021). Middle Miocene temperature and productivity evolution at a Northeast Atlantic Shelf Site (IODP U1318, Porcupine Basin): Global and regional changes. *Paleoceanography and Paleoclimatology*, *36*(7). https://doi.org/10.1029/2020pa004059

Scheiner, F., Holcová, K., Milovský, R., & Kuhnert, H. (2018). Temperature and isotopic composition of seawater in the epicontinental sea (Central Paratethys) during the middle Miocene climate transition based on Mg/Ca, δ 18 O and δ 13 C from foraminiferal tests. *Palaeogeography, Palaeoclimatology, Palaeoecology*, *495*, 60–71. https://doi.org/10.1016/j.palaeo.2017.12.027

Seki, O., Schmidt, D. N., Schouten, S., Hopmans, E. C., Damsté, S. J. S., & Pancost, R. D. (2012). Paleoceanographic changes in the Eastern Equatorial Pacific over the last 10 Myr. *Paleoceanography*, *27*(3). https://doi.org/10.1029/2011pa002158

Sosdian, S. M., & Lear, C. H. (2020). Initiation of the Western Pacific warm pool at the middle Miocene climate transition? *Paleoceanography and Paleoclimatology*, *35*(12), e2020PA003920. https://doi.org/10.1029/2020pa003920

Steinke, S., Groeneveld, J., Johnstone, H., & Rendle-Bühring, R. (2010). East Asian summer monsoon weakening after 7.5Ma: Evidence from combined planktonic foraminifera Mg/Ca and δ18O (ODP Site 1146; northern South China Sea). *Palaeogeography, Palaeoclimatology, Palaeoecology*, *289*(1–4), 33–43. https://doi.org/10.1016/j.palaeo.2010.02.007

Tzanova, A., Herbert, T. D., & Peterson, L. (2015). Cooling Mediterranean Sea surface temperatures during the Late Miocene provide a climate context for evolutionary transitions in Africa and Eurasia. *Earth and Planetary Science Letters*, *419*, 71–80. https://doi.org/10.1016/j.epsl.2015.03.016

Wolfe, J. A. (2013). Distribution of major vegetational types during the tertiary. *Geophysical Monograph Serie*s, 357–375. https://doi.org/10.1029/gm032p0357

Zhang, Y. G., Pagani, M., & Liu, Z. (2014). A 12-million-year temperature history of the Tropical Pacific Ocean. *Science*, *344*(6179), 84–87. https://doi.org/10.1126/science.1246172

Zhang, Y. G., Pagani, M., Liu, Z., Bohaty, S. M., & De Conto, R. (2013). A 40-million-year history of atmospheric CO_2. *Philosophical Transactions of the Royal Society A: Mathematical, Physical and Engineering Sciences*, *371*(2001), 20130096. https://doi.org/10.1098/rsta.2013.0096

Zhuang, G., Pagani, M., & Zhang, Y. G. (2017). Monsoonal upwelling in the Western Arabian Sea since the middle Miocene. *Geology*, *45*(7), 655–658. https://doi.org/10.1130/g39013.1

Erratum

In the originally published version of this article, the following sentence in the caption to figure 8 contained an error: “Zonal mean SIC of Miocene experiments shown as (b) annual (top row), (d) DJF, () MAM, (i) JJA and (j) SON.” The sentence has been corrected to read “Zonal mean SIC of Miocene experiments shown as (b) annual mean, (d) DJF, (f) MAM, (h) JJA and (j) SON.” This may be considered the authoritative version of record.